

1 Highlights

2 **Testing tholins as analogues of the dark reddish material covering Pluto's Cthulhu** 3 **region**

4 M. Fayolle, E. Quirico, B. Schmitt, L. Jovanovic, T. Gautier, N. Carrasco, W. Grundy, V. Vuitton, O. Poch, S.
5 Protopapa, L. Young, D. Cruikshank, C. Dalle Ore, T. Bertrand, A. Stern, the New Horizons Surface Composi-
6 tion Science Theme Team.

- 7 • New Horizons' reflectance spectra of the Cthulhu dark belt of Pluto were modelled with tholins.
- 8 • Reflectance factors, phase function and optical constants of these tholins were numerically determined
9 from tholins' reflectance measurements.
- 10 • Tholins do not reproduce the featureless spectra of Cthulhu.
- 11 • These results could suggest that this region is covered with a highly porous layer of organic aerosols.

Testing tholins as analogues of the dark reddish material covering Pluto's Cthulhu region

M. Fayolle^{a,b,*,1}, E. Quirico^a, B. Schmitt^a, L. Jovanovic^c, T. Gautier^c, N. Carrasco^c, W. Grundy^d, V. Vuitton^a, O. Poch^a, S. Protopapa^e, L. Young^e, D. Cruikshank^f, C. Dalle Ore^f, T. Bertrand^{f,g}, A. Stern^e and the New Horizons Surface Composition Science Theme Team.

^a Université Grenoble Alpes, CNRS, CNES, IPAG, France

^b Delft University of Technology, 2629 HS Delft, The Netherlands

^c Université Paris-Saclay, UVSQ, CNRS, Sorbonne Université, LATMOS, 78280, Guyancourt, France

^d Lowell Observatory Flagstaff, AZ 86001, USA

^e Southwest Research Institute Boulder, CO 80302, USA

^f Ames Research Center, Space Science Division, National Aeronautics and Space Administration (NASA), Moffett Field, CA, USA

^g Laboratoire de Météorologie Dynamique, IPSL, Sorbonne Universités, UPMC Université Paris 06, CNRS, BP99, 75005 Paris, France.

ARTICLE INFO

Keywords:

New Horizons

Pluto's Cthulhu region

Tholins


Radiative transfer

ABSTRACT

Pluto's fly-by by the New Horizons spacecraft in July 2015 has revealed a dark reddish equatorial region, named Cthulhu, covered by a dark, non-icy material whose origin and composition have yet to be determined. It has been suggested that this material could form from the sedimentation of photochemical aerosols, originating from dissociation and ionisation processes in Pluto's high atmosphere (similarly to aerosols forming Titan's haze). This hypothesis is here further investigated by comparing New Horizons spectra collected both in the visible and the near-infrared to laboratory reflectance measurements of analogues of Pluto's aerosols (Pluto tholins). These aerosols were synthesised in conditions mimicking Pluto's atmosphere, and their optical and reflectance properties were determined, before being used in Hapke models. In particular, the single scattering albedo and phase function of Pluto tholins were retrieved through Hapke model inversion, performed from laboratory reflectance spectra collected under various geometries. From reconstructed reflectance spectra and direct comparison with New Horizons data, some of these tholins are shown to reproduce the photometric level (*i.e.* [reflectance continuum](#)) reasonably well in the near-infrared. Nevertheless, a misfit of the red visible slope still remains and tholins absorption bands present in the modelled spectra are absent in those collected by the New Horizons instruments. Several hypotheses are considered to explain the absence of these absorption features in LEISA data, namely high porosity effects or GCR irradiation. The formation of highly porous structures, which is currently our preferred scenario, could be promoted by either sublimation of ices initially mixed with the aerosols, or gentle deposition under Pluto's weak gravity.

1. Introduction

Pluto is the largest of the Trans-Neptunian objects (TNOs). Before the flyby performed by the New Horizons' spacecraft in July, 2015, knowledge of Pluto's surface composition was limited to ground-based and Hubble Space Telescope (HST), disk-integrated observations. However, inferring Pluto's surface composition is of primary importance to gain insight into its bulk composition and to understand the interactions between the surface and Pluto's tenuous atmosphere. Before the New Horizons mission, CH₄ (Cruikshank et al., 1976), N₂ and CO ices (Owen et al., 1993) were identified from ground-based measurements, while the presence of water ice was expected but not firmly confirmed (Grundy and Buie, 2002). Ground-based

 m.s.fayolle@tudelft.nl (M. Fayolle)

ORCID(S): 0000-0003-4407-5031 (M. Fayolle)

63 spectra also contain indications of the presence of C₂H₆ ice (Nakamura et al., 2000; Sasaki et al., 2004;
 64 Cruikshank et al., 2006; DeMeo et al., 2010; Holler et al., 2014), and possibly of nitriles (Protopapa et al.,
 65 2008). Not only the spectrophotometric data collected during Pluto's flyby confirmed the presence of CH₄,
 66 N₂, CO and H₂O-ice on the surface (Grundy et al., 2016; Schmitt et al., 2017; Protopapa et al., 2017), but
 67 they also showed possible evidence for methanol CH₃OH ice (Cook et al., 2019).

68 In addition to bright terrains covered by volatile ices, dark regions were already detected by ground-based
 69 and HST observations (*e.g.* Buie and Tholen, 1989; Buie et al., 2010; Grundy and Buie, 2002) and were later
 70 confirmed by the New Horizons' flyby (Grundy et al., 2016; Olkin et al., 2017; Protopapa et al., 2020). These
 71 regions are extremely low reflectance terrains showing a steep red slope in the visible. This advocates for
 72 the presence of a non-icy, dark material on Pluto's surface which has not yet been firmly identified. Most of
 73 these low reflectance terrains are dark red patchy regions located along Pluto's equatorial belt. The largest
 74 of these dark red patches, which extends from about 20° east to 160° east in longitude, is referred to as the
 75 Cthulhu region, and presents some of the reddest colors of Pluto's surface. Three main scenarios currently
 76 coexist to explain the presence of this dark material on the surface of Pluto.

77 First, this material could originate from the formation of the planet itself (Sekine et al., 2017). Pluto
 78 is thought to have formed from a giant impact that might have also created its satellite Charon (Canup,
 79 2010; Desch, 2015; McKinnon et al., 2017). The extremely high energy delivered by such a collision between
 80 the proto-Pluto and the impactor is suspected to have triggered the melting of a significant part of the
 81 surface and icy-bedrock, creating a warm liquid water ocean. It has been shown that dark reddish, organic
 82 material can be synthesised in warm liquid water from simple organic compounds (*e.g.* formaldehyde)
 83 that are typically found in comets and could have been present on the proto-Pluto or brought in by the
 84 impactor (Sekine et al., 2017). Polymerization of the simple organic compounds would lead to the formation
 85 of complex macromolecular compounds, responsible for the darkening and reddening of the water solution.
 86 Sample materials formed in warm water solution showed a steep red slope in the visible and no strong spectral
 87 feature in the near-infrared, which seems consistent with the New Horizons spectra collected over the dark
 88 red equatorial regions of Pluto (Sekine et al., 2017). Moreover, hydrodynamics simulation conducted in
 89 Sekine et al. (2017) shows that significant melted basins could have been created by a giant impact, the size
 90 of the largest one being comparable to that of the Cthulhu region.

91 Second, it has also been proposed that the red material could originate from the irradiation of ices on
 92 Pluto's surface by solar ultraviolet (UV) light and galactic cosmic rays (GCR), with a small contribution
 93 from charged solar wind particles (Cruikshank et al., 2015). [As Pluto's tenuous atmosphere may have
 94 blocked most of the UV flux in the past](#), GCR was considered a more likely candidate, even if its energy
 95 flux at Pluto's distance is significantly lower than that of UV light. Laboratory experiments showed that
 96 both UV and charged particles irradiation of a mixture of the different ices present on Pluto (CH₄, N₂, CO,
 97 C₂H₆) can trigger a rich chemistry and form a complex refractory residue that might account for the dark,
 98 non-icy material on the surface (see review in Cruikshank et al., 2015).

99 Finally, the last hypothesis identifies the dark red material covering the low reflectance terrains of Pluto
 100 as haze particles deposited onto the surface. A layered haze extending up to about 350 km above the surface
 101 has been discovered by the New Horizons spacecraft during its flyby (*e.g.* Gladstone et al., 2016; Grundy
 102 et al., 2018; Young et al., 2018). Haze particles originate from the dissociation and ionisation of Pluto's
 103 upper atmosphere gases (CH₄, N₂, and CO) due to radiolysis and photolysis processes. Different energetic
 104 sources are possible drivers for the haze production (*e.g.* Cheng et al., 2017; Grundy et al., 2018). First,
 105 photons originating from the Sun are an important energy source. Ly- α photons are energetic enough to
 106 break C-H bonds in CH₄ and their fluxes are relatively high. Although more energetic photons are present in
 107 smaller quantities than Ly- α photons, they also contribute to photolysis and are able to break the stronger
 108 triple bonds in N₂ and CO gases. In addition to photons, protons and electrons originating from the Sun
 109 are also expected to trigger gases dissociation in Pluto's upper atmosphere. Finally, cosmic rays also play a
 110 role despite their low fluxes at Pluto's distance, as they deliver highly energetic particles.

111 The formation of haze particles starts in the upper layers of Pluto's atmosphere, where dissociation
 112 products (ions, radicals) accrete and build larger and more complex molecules. Other gases like HCN,
 113 C₂H₂, or H₂O can stick to the haze particles, either being adsorbed, chemically bonded, or directly condensed
 114 around the haze particle (*e.g.* Luspay-Kuti et al., 2017; Gao et al., 2017; Wong et al., 2017). When growing,
 115 the haze particles also become heavier and start falling down. The temperature rises as they reach lower

altitudes, initiating sublimation of the most volatile constituents of the haze particles.

The analysis of combined MVIC and LEISA over both Cthulhu and Lowell regions by Protopapa et al. (2020) showed that a single colouring agent could account for the diversity of Pluto's surface colours. The different colours are likely to be caused by changes in abundance and particle size of a single material, quite similar to Khare's Titan tholins. Although this does not discard the other scenarios, it supports the hypothesis of an atmospheric origin for Pluto's dark material.

This paper further investigates this hypothesis, by analysing whether analogues of the haze particles forming in Pluto's atmosphere could reproduce the reddest colours observed on the surface. The spectral reflectance properties of the analogues (so-called tholins, as introduced in Sagan and Khare, 1979) were measured through spectro-gonio-radiometry, and were then fitted to the spectra collected by the Ralph instrument of the New Horizons spacecraft during its flyby of Pluto.

The New Horizons spectrophotometric observations are first presented in Section 2, while the experimental setups used to synthesise the analogues of Pluto's haze particles and measure their reflectance spectra are described in Section 3. The numerical models used to simulate the surface reflectance are then detailed in Section 4. The experimental results are provided in Section 5, where the optical properties of the Pluto tholins are analysed. Section 6 presents the comparison with respect to New Horizons data. Finally, results are discussed in Section 7 and the main concluding points are summarised in Section 8.

2. New Horizons observations

Pluto's flyby performed by the New Horizons spacecraft occurred in July 2015, the point of closest approach having been reached on July, 14th after about 10 years of travel in space (Stern et al., 2015). The composition of Pluto's surface was investigated through observations collected by the Ralph instrument (Reuter et al., 2008). It combines a visible and near-infrared camera (MVIC) and an infrared imaging spectrometer (LEISA).

2.1. Measurements

MVIC possesses four spectral channels, the first three being referred to as the BLUE filter (covering a spectral range extending from $0.40 \mu\text{m}$ to $0.55 \mu\text{m}$), the RED filter (from $0.54 \mu\text{m}$ to $0.70 \mu\text{m}$), and the NIR (near-infrared) filter (from $0.78 \mu\text{m}$ to $0.98 \mu\text{m}$), respectively. Additionally, one channel covering wavelengths from $0.86 \mu\text{m}$ to $0.98 \mu\text{m}$ is dedicated to the detection of the narrow CH_4 band present in this specific spectral range.

The LEISA instrument covers a spectral range going from $1.25 \mu\text{m}$ to $2.50 \mu\text{m}$. Most of the chemical components expected to be present on Pluto's surface show absorption features in this spectral range, thus making LEISA data able to verify their identification. The spectral resolution of the LEISA instrument is $\lambda/\Delta\lambda = 240$ between $1.25 \mu\text{m}$ and $2.50 \mu\text{m}$. A higher spectral resolution ($\lambda/\Delta\lambda = 560$) was supposed to be available from $2.1 \mu\text{m}$ to $2.25 \mu\text{m}$, but this higher resolution segment turned out to be difficult to calibrate properly. Therefore, this work focuses on the lower spectral resolution segment only.

The maps generated by the LEISA instrument comprise a spectral dimension and a spatial one. The near-infrared spectrum from $1.25 \mu\text{m}$ to $2.5 \mu\text{m}$ is obtained along the in-track direction. The reflectance of different parts of the surface is theoretically measured at the same wavelength in the cross-track direction. By scanning the image in the in-track direction, and thus at different wavelengths, the full spectrum of a given region of Pluto can be constructed. However, due to slight instrumental effects, the measurements are not exactly conducted at the same wavelength in the cross-track direction. A so-called "spectral smile" of a few spectels is present over the 256 pixels array along the cross-track direction. During the scanning of the target by LEISA, the spacecraft kept rotating around its z-axis so that Pluto's surface is scanned in the transmission band pass direction (in-track direction). It also tries to compensate any shift of the scan in the perpendicular direction with brief thruster bursts. These zig-zag scans have to be corrected during data projection.

2.2. Data pre-processing

Both photometric and spectral calibrations of the Ralph instrument were conducted before the launch of the spacecraft and completed with in-flight calibrations with respect to stars. An additional "flat-field"

165 calibration was performed, based on a rapid scan of Pluto's surface in the cross-track direction (as opposed
 166 to the in-track direction which is the nominal orientation of the instrument when collecting observations).
 167 Each pixel of the 256 pixels array thus covers almost the same part of the surface. The overall calibration of
 168 LEISA data is based on a combination of those ground-based and in-flight stellar calibrations, spectral smile
 169 corrections, and flat fielding. Nonetheless, some calibration issues remain in New Horizons data. The LEISA
 170 reflectance values are overestimated by an amount of 26% and should therefore be scaled down accordingly
 171 (Protopapa et al., 2020).

172 Several scans of Pluto's surface by the LEISA instrument were conducted, and data cubes were re-
 173 constructed with the Integrated Software for Imagers and Spectrometers (ISIS) software from the United
 174 States Geological Survey (USGS). Two of the close-encounter data cubes were calibrated, and projected
 175 onto LORRI Pluto-sized spherical data map (orthographic projection at same observation geometry). Sharp
 176 geological features identifiable in both LORRI and LEISA data were finally used for slight mismatch cor-
 177 rections in LEISA data projection, with respect to the higher resolution LORRI base map. Together, the
 178 two calibrated LEISA data cubes cover the whole visible disk of the planet.

179 In this work, we used the same calibrated data cube covering Cthulhu region as in Schmitt et al. (2017).
 180 This data cube does not consist of raw data but follows from a Principal Component Analysis (PCA),
 181 described in more details in Schmitt et al. (2017). This post-processing step aims at identifying the main
 182 surface components, as well as mapping their distribution, and removing most of the instrumental effects
 183 and noise. The result of the PCA was that the first nine Principal Components account for almost 95% of
 184 the variance, demonstrating the good quality of LEISA data. Reduced-noise data cubes were reconstructed
 185 from a PCA inversion, by assuming that the first Principal Components account for the major part of the
 186 variance. Using these reduced-noise data cubes instead of the raw ones allows for a sharper analysis of New
 187 Horizons spectra collected over the Cthulhu region.

188 The LEISA data from the reconstructed cube covering Cthulhu region were scaled down by 26% to
 189 correct the calibration issues previously mentioned. [A precise and reliable value for the uncertainty of this
 190 calibration factor is hard to determine. We however used 7% as a conservative estimate for MVIC data
 191 error bars. This value is based on the comparison of two independent calibration methods for MVIC data
 192 in Howett et al. \(2017\). Discrepancies in the correction factor are limited to 3-7%, such that 7% seemed a
 193 reasonable upper limit for the uncertainty value.](#) Finally, MVIC data were corrected to LEISA geometry,
 194 following the method presented in Protopapa et al. (2020).

195 2.3. Cthulhu spectra

196 To identify the red dark material covering Cthulhu, New Horizons spectra collected over this specific
 197 region were extracted from the data cube described above. The main focus of this study is on the core of
 198 the Cthulhu region, where the dark organic material is supposed to be the most concentrated. A spatial
 199 average was then computed over several pixels which were identified as the end-member of the red material in
 200 Schmitt et al. (2017). Using the averaged spectrum as a reference for comparison with laboratory reflectance
 201 measurements allows to further reduce the pixel-to-pixel noise of the New Horizons spectrum.

202 The MVIC data and LEISA reflectance spectrum of the red material's end-member are reproduced in
 203 Figure 1. In addition to the dark material end-member spectrum, we also used an average spectrum collected
 204 in the eastern periphery of Cthulhu. This spectrum exhibits strong absorption bands at 1.5 μm and 2.0
 205 μm , demonstrating the presence of water ice mixed with the dark material. Evidences of a gradient in H_2O
 206 concentration from the center to the periphery of Cthulhu were already brought in Schmitt et al. (2017).

207 Because the reflectance level is highly dependent on the illumination and observation geometry under
 208 which a spectrum is collected, the average geometries corresponding to our two spectra of interest were
 209 retrieved. They are reported in Table 1, along with the average coordinates of the two regions over which
 210 these spectra were obtained.

211 3. Experimental setup

212 The way Pluto tholins are synthesised is first described in Section 3.1, before presenting the experimental
 213 setup used to conduct the laboratory reflectance measurements in Section 3.2.

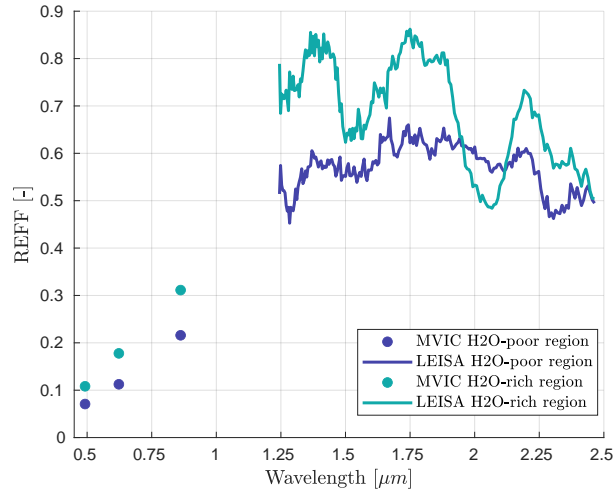


Figure 1: New Horizons reflectance spectra. The light and dark blue curves correspond to New Horizons LEISA spectra collected over H₂O-rich and H₂O-poor eastern regions of Cthulhu, respectively. They are retrieved from the reconstructed data cube described in Section 2.2. MVIC data are corrected to LEISA geometry (see Protopapa et al., 2020).

	Nb pixels [-]	Lat. [°]	Long. [°]
H₂O-poor region	47	158.8E	2.6S
H₂O-rich region	30	152.9E	13.8S

	<i>i</i> [°]	<i>e</i> [°]	<i>g</i> [°]
H₂O-poor region	58.6	41.0	22.6
H₂O-rich region	67.7	52.6	22.5

Table 1: Average coordinates and viewing geometry of the two regions of interest for this study (H₂O-poor and H₂O-rich regions of Cthulhu), over which the New Horizons spectra displayed in Figure 1 were retrieved and averaged.

3.1. Tholins synthesis

Pluto tholins were synthesised in LATMOS (French acronym for Laboratoire Atmosphères, Milieux, Observations Spatiales), with the PAMPRE experimental setup (Production d'Aérosols en Microgravité par Plasma REactif, for more details see *e.g.* Szopa et al., 2006; Alcouffe et al., 2009; Jovanović et al., 2020). It was first designed to synthesise laboratory analogues for Titan's haze particles, from an initial gas mixture of N₂ and CH₄. For this study, it was used to produce analogues of Pluto's haze particles, by adding CO to the N₂:CH₄ gas mixture (Lellouch et al., 2017; Young et al., 2018). PAMPRE simulates the dissociation of gases molecules as it occurs in Titan's or Pluto's high atmospheres, due to UV light or energetic particles. In the PAMPRE setup, the molecules are dissociated in a cold plasma discharge between two electrodes. Dissociation products evolve into more complex products. As they grow, they become heavier and are finally recovered as a dusty material made of small spherical particles. The synthesis is conducted at low pressure (0.9 ± 0.1 mbar) and room temperature.

To synthesise Pluto tholins, two initial gas compositions were used: N₂:CH₄ = 99%:1% and N₂:CH₄ = 95%:5%, with 500 ppm of CO being added to each of them. They are thought to be representative of Pluto's atmosphere composition at altitudes of 400 and 650 km, respectively (Lellouch et al., 2017; Young et al., 2018). Their chemical composition was studied in Jovanović et al. (2020), and their optical properties in Jovanović et al. (2021).

In the following, for the sake of conciseness, these two types of Pluto tholins are referred to as 5%CH₄ and 1%CH₄ tholins, since the relative amount of CH₄ drives the reflectance differences between them (see discussion in Section 6.1.2). Small quantities of these Pluto tholins were also mixed with pyrrhotite, an opaque mineral used here as a darkening agent to model the effect of contamination by dark interplanetary

235 dust (see discussion in Section 7).

236 3.2. Laboratory reflectance measurements

237 The spectrophotometric properties of the tholins samples were investigated by measuring their reflectance
 238 at various geometries with a spectro-gonio-radiometer developed at IPAG: the Spectro-photometer with
 239 cHanging Angles for Detection Of Weak Signals (SHADOWS) (Potin et al., 2018). This instrument operates
 240 in the 0.4-4.8 μm spectral range and thus covers the full spectral range of the New Horizons observations
 241 both in the visible and in the near-infrared (from 0.4 μm to 2.5 μm), with an absolute photometric accuracy
 242 better than 1%. It therefore allows for a direct comparison between laboratory measurements and spectra
 243 collected by the New Horizons spacecraft.

244 The spectro-gonio-radiometer can perform reflectance measurements under various illumination and ob-
 245 servation geometries. The geometry under which the spectrophotometric measurements are conducted sig-
 246 nificantly affects both the reflectance level and the spectral contrast (Hapke, 2012b). To compare the spectra
 247 measured in the laboratory on synthesised samples with those collected by New Horizons, the illumination
 248 and observation geometries must therefore be as similar as possible. This is necessary to remove any varia-
 249 tion of the reflectance induced by a geometry difference and not by the reflectance properties of the material
 250 itself.

251 Nonetheless, first measuring the reflectance spectra of the tholins samples under a larger range of il-
 252 lumination and observation geometries allows to characterise the photometric function of the samples, as
 253 well as the evolution of their absorption features as a function of the geometry. This is crucial to retrieve
 254 tholins' optical properties from their reflectance measurements for modelling purposes (see Section 5.5). The
 255 reflectance measurements were conducted under incidence angles of 0°, 30°, and 60°, and emergence angles
 256 ranging from -70° to 70° with a step of 10°.

257 Some additional measurements were carried out under vacuum and with progressive heating of the
 258 samples (up to 100°C), to verify that the observed absorption features were not caused by adsorbed water.

259 All data are made available through the GhoSST database in SSHADE infrastructure of solid spec-
 260 troscopy: https://doi.org/10.26302/SSHADE/EXPERIMENT_BS_20201201_001 (Fayolle et al., 2018).

261 4. Numerical models

262 Complementing the laboratory reflectance measurements, an analytical model was used to simulate the
 263 reflectance spectra of Cthulhu's surface. Section 4.1 first discusses the reflectance model, while Section 4.2
 264 describes the modelling of the surface itself.

265 4.1. Reflectance model

266 4.1.1. Nominal Hapke model

267 In this work, the Hapke model was selected, as one of the most complete theoretical model currently
 268 available to simulate surfaces' reflectance (*e.g.* Hapke, 1986, 1993, 2002, 2008, 2012a,b). The complete
 269 formulation of the Hapke model is given as follows:

$$\begin{aligned}
 r(i, e, g, \lambda) &= K \frac{\omega(\lambda)}{4\pi} \frac{\mu_{0e}}{\mu_{0e} + \mu_e} \\
 &\times \left[P(g, \lambda) (1 + B_{SH}(g)) + H\left(\frac{\mu_{0e}}{K}\right) H\left(\frac{\mu_e}{K}\right) - 1 \right] \\
 &\times (1 + B_{CB}(g)) S(i, e, g, \bar{\theta}),
 \end{aligned} \tag{1}$$

270 with $\mu_{0e} = \cos(i_e)$ and $\mu_e = \cos(e_e)$. The reflectance r is given as a function of the illumination and
 271 observation geometry angles i , e , and g (incidence, emergence, and phase angles respectively), and of various
 272 parameters describing the surface properties. The angles i_e and e_e refer to the incidence and emergence
 273 angles corrected for roughness. The porosity and macroscopic roughness of the surface are both taken into
 274 account (parameters K and $\bar{\theta}$, respectively). The shadowing function S describes how shadows are cast
 275 on the surface particles, and the resulting change in the total reflectance. It accounts for the effect of the
 276 macroscopic roughness $\bar{\theta}$ at a given illumination and observation geometry. The brightness growth observed

at very small phase angles is described by the two opposition effect terms: B_{SH} and B_{CB} , representing the shadow hiding and coherent backscattering opposition effects, respectively. Multiple scattering is accounted for in the H function. Finally, the phase function $P(g, \lambda)$ describes the dependency of the photometric level to the phase angle g .

The spectral information is carried out by the single scattering albedo ω . Its value depends on the mean particle diameter D , wavelength λ , and optical constants n and k (real and imaginary parts of the dielectric constant ϵ , respectively), as follows (Hapke, 2012b):

$$\omega = Q_S/Q_E = S_e + (1 - S_e) \frac{1 - S_i}{1 - S_i \Theta} \Theta, \quad (2)$$

$$\text{with } S_e = \frac{(n-1)^2 + k^2}{(n+1)^2 + k^2} + 0.05, \quad (3)$$

$$S_i = 1 - \frac{4}{n(n+1)^2}, \quad (4)$$

$$\Theta = e^{-\alpha \bar{D}}, \quad (5)$$

$$\bar{D} = \frac{2}{3} \left[n^2 - \frac{1}{n} (n^2 - 1)^{3/2} \right] D. \quad (6)$$

Equation 2 only holds if the particle mean diameter D meets the condition $D\pi \geq \lambda$. More precisely, when the particle diameter becomes comparable or smaller than the wavelength λ , the expression of the single scattering albedo is modified to account for a change of scattering regime (Rayleigh scattering, see *e.g.* Hapke, 2012b). The single scattering albedo is then

$$\omega = Q_S/Q_E,$$

with

$$Q_E = \frac{24nk}{(n^2 + k^2)^2 + 4(n^2 - k^2) + 4} \left(\frac{\pi D}{\lambda} \right), \quad (7)$$

$$Q_S = \frac{8}{3} \frac{[(n^2 + k^2)^2 + n^2 - k^2 - 2]^2 + 36n^2k^2}{[(n^2 + k^2)^2 + 4(n^2 - k^2) + 4]^2} \left(\frac{\pi D}{\lambda} \right)^4. \quad (8)$$

4.1.2. Simplified reflectance model

Additional assumptions were made to simplify the complete formulation of the Hapke model given in Equation 1. Over the Cthulhu region, New Horizons spectra were collected at phase angles close to 22° (Table 1). The contribution of the coherent backscattering opposition effect term in the reflectance model can thus be safely neglected. Indeed, this effect generally only manifests itself for phase angles smaller than 2° (Hapke, 2002).

The multiple scattering function H is still included in our simplified version of Hapke model (analytical expressions for H can be found in Hapke, 2012b). The reflectance measurements performed on Pluto tholins indeed showed that they are extremely bright in the near-infrared. Multiple scattering cannot be neglected in that case since the absorption might not be efficient enough to ensure that the incident light is fully absorbed after encountering a single particle.

Finally, a macroscopic roughness of 20° was assumed for the shadowing function $S(i, e, g, \bar{\theta})$, which is the value derived from Hapke model's fit of the phase curve obtained during 2018 Pluto's occultation (Verbiscer et al., 2019).

4.2. Surface modelling

4.2.1. Surface constituents

The low reflectance terrains of Pluto are not only covered by a dark red organic material. As already discussed in Section 2.3, water was identified towards the periphery of Cthulhu, where the dark material is

307 probably mixed within H₂O ice. CH₄ was also detected on the topographic heights of Cthulhu and could
 308 correspond to seasonal deposits only subsisting at high altitudes. CH₄ ice could also be present in the
 309 bedrock of Pluto, along with H₂O which is a potential bedrock constituent (Grundy et al., 2018). Addi-
 310 tionally, tentative evidences for hydrocarbon-rich ices in Cthulhu region were brought in Cook et al. (2019).
 311 Hydrocarbon-rich species were also mentioned as photochemical products participating in the formation of
 312 haze particles in Pluto's atmosphere in Grundy et al. (2018).

313 The model of Pluto's surface proposed in this work is thus a mixture of the above-mentioned icy species,
 314 namely H₂O, CH₄, as well as CH₃OH and C₂H₆ which were selected as representative for the potential
 315 hydrocarbon species present in Cthulhu. Pluto tholins were added, as analogues for the dark-red organic
 316 material.

317 4.2.2. Intimate mixing between refractory species

318 A simple mixing model representing the surface as a spatial mixing between two separate units was first
 319 considered (represented in Figure 2). The first unit contains the volatile species (here CH₄) while the second
 320 one is composed of the refractories (tholins, H₂O, CH₃OH, and C₂H₆).

321 The total reflectance of the surface is calculated as the sum of the reflectance of the two units, weighted
 322 by their relative spatial ratio (left as an unknown in our model). Within the refractory unit, it was assumed
 323 that the different species are mixed at the individual particle scale. The reflectance of such an intimate,
 324 homogeneous mixture between various chemical compounds is modelled from an averaged single scattering
 325 albedo and phase function. These averaged values are computed from the individual properties of the
 326 different compounds involved in the mixing (relative mass ratio m_j , density ρ_j , particle mean diameter D_j
 327 and single scattering albedo ω_j), as follows:

$$\omega = \left(\sum_j \frac{m_j \omega_j}{\rho_j D_j} \right) / \left(\sum_j \frac{m_j}{\rho_j D_j} \right). \quad (9)$$

328 4.2.3. Ices condensed on tholins particles

329 A second mixing model was also considered, which is thought to be more representative of the way haze
 330 particles form in Pluto's atmosphere. As haze particles grow and fall down to the surface, ices can condense
 331 around them (*e.g.* Luspay-Kuti et al., 2017; Gao et al., 2017; Wong et al., 2017). The particles then sediment
 332 and settle onto Pluto's surface, forming an intimate mixture of tholins surrounded by various ices.

333 With this surface model, tholins are thus not directly mixed with icy components, but rather trapped
 334 into icy particles which are intimately mixed with each other. Tholins act as a colouring pigment in an icy
 335 matrix. To simulate the reflectance of ices condensed around tholins particles, Maxwell-Garnett effective
 336 medium model was applied. The use of this model is justified by the fact that the tholins particles are
 337 smaller than the wavelength. The effective dielectric constant ϵ_{eff} can be deduced from those of the matrix
 338 and of the inclusions, and is given by

$$\epsilon_{\text{eff}} = \epsilon_1 + 3p\epsilon_1 \frac{\epsilon_2 - \epsilon_1}{\epsilon_2 + 2\epsilon_1 - p(\epsilon_2 - \epsilon_1)}, \quad (10)$$

339 where p is the fraction of the embedded material among the matrix, while ϵ_1 and ϵ_2 refer to the dielectric
 340 constant of the matrix and of the embedded material, respectively. The effective optical constants of such a
 341 medium can be directly retrieved as the real and imaginary parts of the dielectric constant, as follows:

$$n_{\text{eff}} = \text{Re}(\epsilon_{\text{eff}}), \quad (11)$$

$$k_{\text{eff}} = \text{Im}(\epsilon_{\text{eff}}). \quad (12)$$

342 The effective optical constants were thus computed for tholins surrounded by various ices, and an intimate
 343 mixing was assumed between the different condensed ice particles. Still, a spatial mixing was modelled
 344 between one spatial unit covered by intimately mixed H₂O, C₂H₆ and CH₃OH icy particles condensed

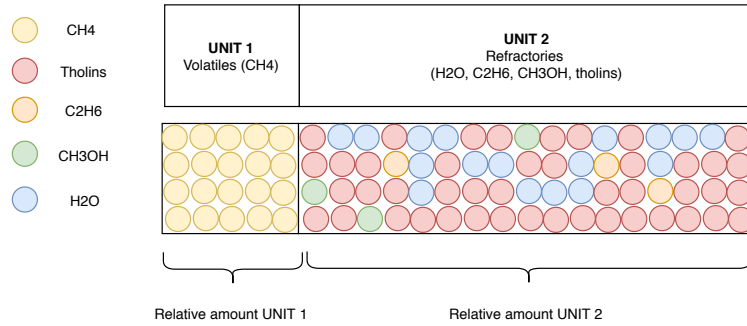


Figure 2: First surface model: spatial mixing between volatiles and refractories, the latter being intimately mixed together.

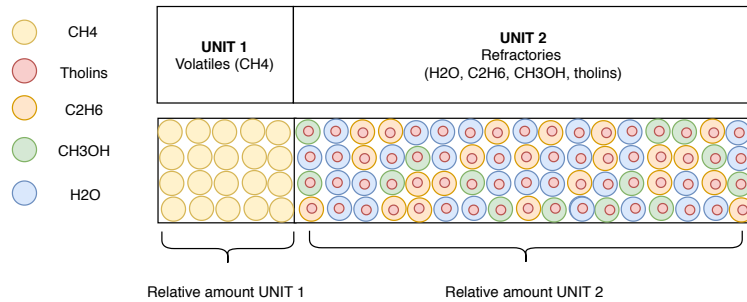


Figure 3: Second surface model: spatial mixing between volatiles and refractories, the latter being composed of ices condensed on tholins particles.

345 around core tholins, and a second unit composed of CH₄-ice to account for the possible presence of CH₄-ice
 346 in the bedrock of Pluto. The spatial mixing ratio between the two units is again an unknown of the model.
 347 A schematic representation of this second mixing model is provided in Figure 3.

348 An additional difficulty arises from the use of the Maxwell-Garnett model. While the simplified Hapke
 349 model only requires the single scattering albedo of the Pluto tholins ω_{tholins} , the Maxwell-Garnett model
 350 needs the associated optical constants n_{tholins} and k_{tholins} to compute the effective optical constants (see
 351 Equations 10, 11 and 12). The single scattering albedo of the effective medium is then computed from n_{eff}
 352 and k_{eff} and plugged in the Hapke model to compute the reflectance. However, assuming ω_{tholins} is known,
 353 there is no direct way to uniquely determine n and k from the single scattering albedo, as clearly shown in
 354 Equations 7 and 8.

355 A commonly used trick is to assume n constant and find the wavelength-dependent values of k that
 356 fit the single scattering albedo. However, a constant value for n_{tholins} over our spectral range of interest
 357 seems rather unrealistic considering the strong absorption in the visible, responsible for the observed red
 358 slope. An alternative option is thus to use a set of n values available in the literature which reproduces the
 359 photometric level of the tholins reasonably well. Using those n values, the k values are computed to match
 360 the single scattering albedo, relying on the fact that most of the spectral information is carried by k . This
 361 second method is expected to provide more realistic estimates of tholins optical constants and was therefore
 362 applied in this work, using the values of n provided in Khare et al. (1984) (see Section 5.4 for comparison
 363 of different sets of tholins optical constants). More details about the numerical determination of the optical
 364 constants n and k from ω are given in Appendix A.2.

365 4.3. Fitting the model to the New Horizons observations

366 We tried to reproduce New Horizons spectra using the models presented in Sections 4.1 and 4.2. The
 367 surface was modelled as a mixture between H₂O ice, hydrocarbon-rich ices (*e.g.* C₂H₆, CH₃OH), CH₄ ice and
 368 tholins, as analogues for the dark material covering Cthulhu region. Except for the tholins, optical constants

369 found in the literature were used for the other chemical components: H₂O-ice: Grundy et al. (2018); CH₄-
 370 ice: Grundy et al. (2002); C₂H₆-ice: Quirico and Schmitt (1997); CH₃OH-ice: Trotta (1996); Cook et al.
 371 (2019). Most of these data are available online in the GhoSST database of the SSHADE infrastructure
 372 (www.sshade.eu).

373 For simplification purposes, the single scattering phase function of Cthulhu's surface was assumed to be
 374 isotropic and independent of wavelength (*i.e.* $P(g, \lambda) = 1$). This was mainly motivated by the fact that the
 375 phase functions of the surface constituents are unknown.

376 When computing the reflectance of the modelled surface, many parameters remained unknown, among
 377 which the relative abundance and mean particle diameter of each surface constituent. **The macroscopic**
 378 **porosity parameter K was also left as a free parameter.** An optimisation algorithm was thus applied in
 379 order to find the best fit with respect to the New Horizons spectra.

380 The final objective was to assess the relevance of Pluto tholins as analogues of the dark material covering
 381 Cthulhu region. It was therefore of primary importance to not only match the near-infrared part of the
 382 spectrum but also MVIC data, collected in the visible. The darkest regions of Pluto indeed present a very
 383 strong red slope in the visible which is due to the dark material only, since ices have very high photometric
 384 level in both the visible and the near-infrared. The fit was thus determined by computing the χ^2 with respect
 385 to both MVIC and LEISA data. Because the MVIC instrument only sampled three different wavelengths
 386 and therefore had a much poorer spectral resolution than the near-infrared spectrometer, MVIC data were
 387 weighted to give them as much weight as the whole LEISA spectrum, strongly constraining Cthulhu spectra
 388 in the visible.

389 Different optimisation algorithms were tested and tuned to find the best performing one, both in terms
 390 of convergence and computational effort. A simple genetic algorithm was eventually selected as offering the
 391 best trade-off between these two criteria for our particular problem (see Appendix B for further details on
 392 the optimisation process).

393 It must be stressed that the global optimum was neither targeted nor achieved with the optimisation
 394 process described above. The number of parameters to estimate and the search space were both too large,
 395 and critical information was missing to precisely reproduce the reflectance of Cthulhu's surface. However,
 396 the main interest of this approach was not to estimate the exact amount of tholins and/or icy species present
 397 in the Cthulhu region. It was rather to determine whether modelling the reflectance of tholins mixed with
 398 different ices could help reproducing the spectra collected by the New Horizons spacecraft. This also made
 399 our simplifying assumptions acceptable here (*e.g.* isotropic phase function).

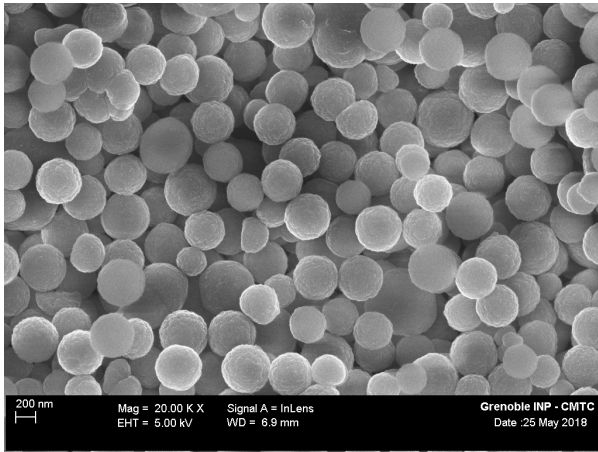
400 5. Experimental results

401 The size and shape of Pluto tholins were first characterised from Scanning Electron Microscopy (SEM)
 402 observations. The laboratory reflectance measurements were then analysed, to better understand the re-
 403 flectance properties of our tholins and thus make the comparison with New Horizons spectrophotometric
 404 data possible.

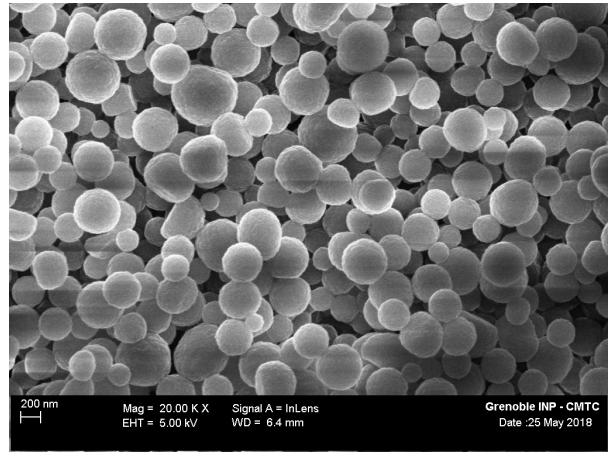
405 5.1. SEM observations

406 The SEM analysis was performed on the two types of Pluto tholins (5%CH₄ and 1%CH₄, respectively),
 407 with the JEOL JSM-840A SEM at University Paris VI and the ZEISS Ultra55 FEG-SEM at CMTC INP
 408 Grenoble operating at 10 kV. It revealed tholins are very regular spherically-shaped particles, which some-
 409 times agglutinate to form larger aggregates. The difference in initial gas mixture composition leads to some
 410 disparities in the physical properties of the synthesised particles. 5%CH₄ tholins overall show more regular
 411 shapes than 1%CH₄ ones. They appear as almost spherical, while the 1%CH₄ tholins particles present more
 412 irregularities, still being spherically-shaped (see Figure 4).

413 From SEM observations, the grain size distribution of Pluto tholins was estimated by measuring the
 414 apparent radius of tholins particles, averaged over a few hundred particles for each of the two tholins
 415 compositions (see Figure 5). The mean radius of both 5%CH₄ and 1%CH₄ tholins particles was estimated
 416 equal to 210 nm although the median is lower, especially for 1%CH₄ tholins (around 200 nm). The grain
 417 size distribution of 5%CH₄ tholins is slightly narrower (standard deviation $\sigma = 35$ nm) than that of the
 418 1%CH₄ tholins ($\sigma = 55$ nm), an observation already made for Titan tholins (Hadamcik et al., 2009). The

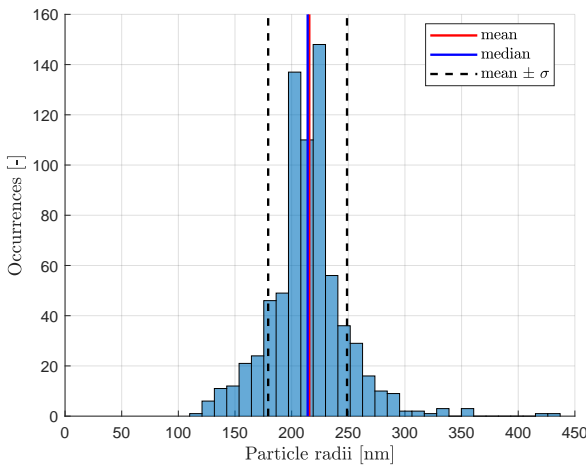


(a) 5%CH₄ tholins.

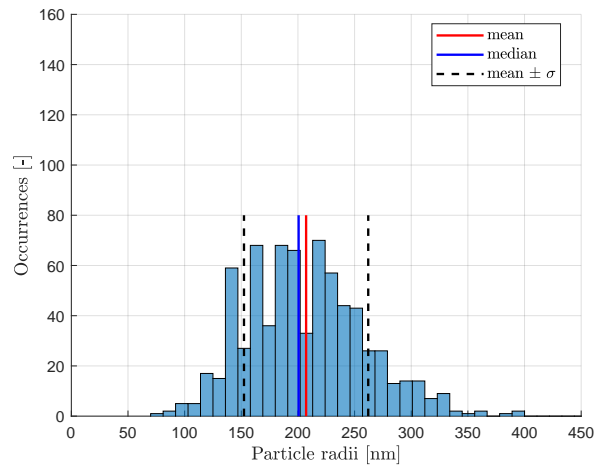


(b) 1%CH₄ tholins.

Figure 4: SEM observations of the two types of Pluto tholins. In both samples, tholins are submicrometer-sized spherical particles. 1%CH₄ tholins however present more irregularities and show more diverse shapes compared to 5%CH₄ tholins. 1%CH₄ tholins also seem to present a wider range of sizes.



(a) 5%CH₄ tholins.



(b) 1%CH₄ tholins.

Figure 5: Grain size distribution derived from SEM observations. Both distributions have an average radius of about 210 nm, although the median is slightly lower for 1%CH₄ tholins (around 200 nm). The size distribution of 1%CH₄ tholins is broader, with a standard deviation of $\sigma = 55$ nm, compared to that of 5%CH₄ tholins ($\sigma = 35$ nm).

419 more irregular shapes of 1%CH₄ tholins might introduce some additional uncertainty in the mean diameter
 420 estimation, but cannot fully account for the much wider dispersion of the mean radius values. The difference
 421 in the dispersion of the grain size distribution is clearly observable even without performing any statistical
 422 analysis from the SEM images (see Figure 4).

423 5.2. Reflectance spectra as a function of the geometry

424 The influence of the illumination and emergence geometry is clearly visible from our laboratory reflectance
 425 measurements. Figure 6 displays the reflectance spectra of 5%CH₄ tholins in the 0.4-2.5 μm range. These
 426 spectra were obtained under a constant incidence angle set to 0°, but with varying emergence angles (ranging
 427 from 10° to 70°), and thus with changing phase angles. The photometric level strongly reduces with increasing
 428 phase angle. However, the absorption features are only slightly affected by the geometry variations, becoming

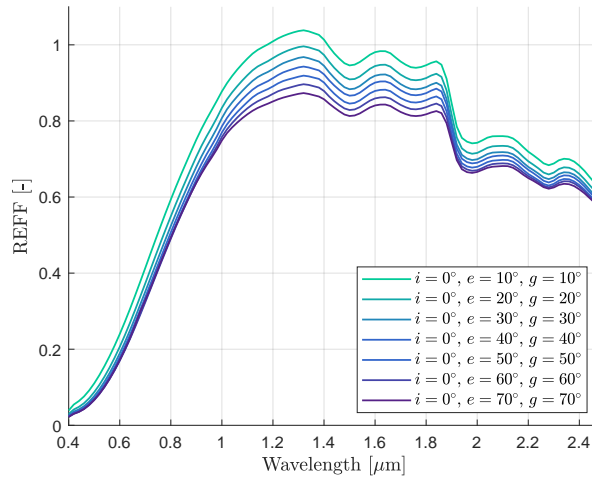


Figure 6: Influence of the observation geometry on the reflectance spectra for 5%CH₄ tholins.

429 shallower when the phase angle increases.

430 Figure 7 also illustrates the evolution of the tholins reflectance with varying incidence and emergence
 431 angles. For each of the three incidence values (0°, 30° and 60°, respectively), the reflectance is displayed as a
 432 function of the emergence angle, for four different wavelengths (all comprised in the New Horizons spectral
 433 range). The tholins tend to reflect the incident light backwards, which is in agreement with the fact that the
 434 reflectance decreases with increasing phase angle. Such a backscattering could possibly be due to the very
 435 small size of the tholins particles (comparable to the wavelength). From both Figures 6 and 7, it is clear
 436 that the observation geometry effects need to be accounted for, and that the comparison between laboratory
 437 measurements and New Horizons data is only meaningful if conducted at similar incidence, emergence and
 438 phase angles.

439 Figures 6 and 7 only display results obtained with the 5%CH₄ tholins but identical reflectance measure-
 440 ments were conducted with the 1%CH₄ sample. There is no noticeable difference between the two types of
 441 Pluto tholins when looking at the photometric behaviour (1%CH₄ tholins are also characterised by a strong
 442 backscattering behaviour). However, the composition of the initial gas mixture of the tholins synthesis has a
 443 strong influence on the shape and absolute level of the reflectance spectra. Both 5%CH₄ and 1%CH₄ tholins'
 444 spectra are provided in Figure 9 (geometry: $i = 0^\circ$, $e = 30^\circ$). Reducing the relative amount of CH₄ in the
 445 synthesis gas darkens the resulting tholins, in agreement with previous findings for Titan tholins (Mahjoub
 446 et al., 2012). 1%CH₄ tholins show a slightly lower reflectance level in the near-infrared. They also exhibit a
 447 more progressive increase of reflectance in the visible, but a steeper slope in the very near-infrared (1.0-1.3
 448 μm). These differences between the two types of tholins become of particular interest when comparing the
 449 laboratory reflectance spectra with New Horizons data (see Section 6).

450 5.3. Photometric and spectral effects of mixing tholins with a darkening agent

451 The deposition and mixture of opaque interplanetary dust grains with the dark red organic material
 452 could darken and change the spectral contrast of Pluto's surface with time. It is thus crucial to quantify the
 453 effect of mixing Pluto tholins with a darkening agent on both the photometric level and spectral contrast.
 454 To this end, the reflectance measurements of Pluto tholins mixed with pyrrhotite (introduced in Section 3.1)
 455 are provided in Figure 8.

456 Figure 8 shows that even extremely small amounts of pyrrhotite strongly darken the tholins after 0.8 μm :
 457 a pyrrhotite/tholins mass ratio of 1/200 decreases the photometric level by about a factor 2 in the near-
 458 infrared. The absorption features are still present and clearly identifiable in the spectra of the darkened
 459 tholins, even for relatively large amounts of pyrrhotite. The implications of these experimental results are
 460 further discussed in Section 7.

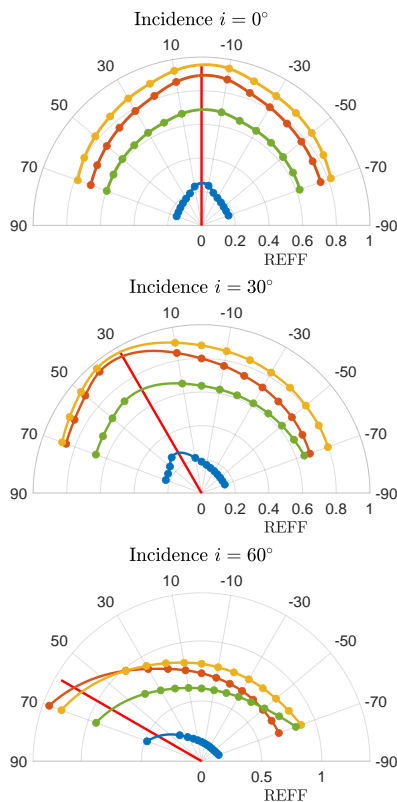


Figure 7: 5%CH₄ tholins reflectance in polar coordinates, for incidences of 0°, 30° and 60° (upper, middle and lower panels respectively), under various emergence angles (from -70° to +70°), and at four different wavelengths: $\lambda = 0.6 \mu\text{m}$ (blue curve), $\lambda = 1.0 \mu\text{m}$ (orange curve), $\lambda = 1.8 \mu\text{m}$ (yellow curve) and $\lambda = 2.4 \mu\text{m}$ (purple curve). The incidence angle is represented by the red line.

5.4. Comparison with optical constants of tholins from literature

We investigated whether optical constants derived for other tholins samples and already available in the literature could be used to reproduce the reflectance of the Pluto tholins analysed in this work. Various types of tholins were previously synthesised and analysed in the literature, mostly to characterize Titan aerosols (Brasse et al., 2015). Multiple techniques exist for the tholins synthesis (*e.g.*, Coll et al., 2013), each of them associated with very different experimental conditions (various temperature and pressure conditions, energy source, gas flow rate, irradiation duration, *etc.*).

The final composition of the tholins particles, and therefore their optical constants, depend on the technique employed to synthesise them. Additionally, the method used to measure the optical constants also influences their values (Brasse et al., 2015). For these reasons, optical constants of tholins available in the literature are very different from one sample and from one measurement technique to another.

An attempt was made to compare the reflectance measurements performed on our N₂:CH₄:CO tholins with spectra calculated from various N₂:CH₄ Titan tholins' optical constants available in the literature (Brasse et al., 2015). Results of this comparison are displayed in Figure 9. It is especially interesting to note that very diverse slopes are obtained in the visible, even between tholins synthesised from initial gas mixtures with similar composition. Unfortunately, none of the available optical constants sets led to a proper fit of our laboratory spectra.

Optical constants presented in Mahjoub et al. (2012) and Sciamma-O'Brien et al. (2012) were determined from tholins synthesised under similar conditions and using the same experimental setup as the Pluto tholins

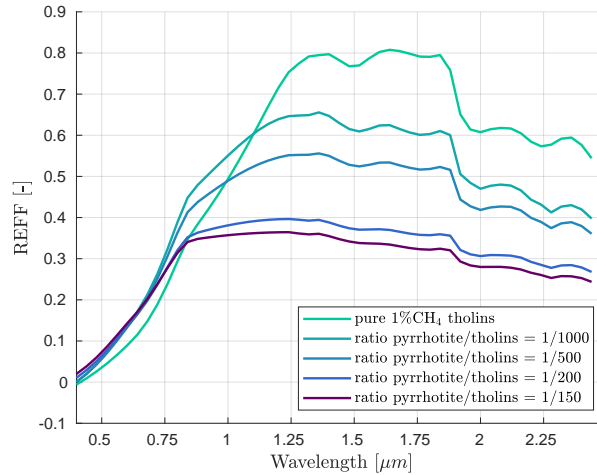


Figure 8: Reflectance computed from inverted single scattering albedo of 1%CH₄ tholins with various pyrrhotite mixing mass ratios ($i = 0^\circ$, $e = 30^\circ$, $g = 30^\circ$, $D = 400$ nm, $P = 1$, $K = 1$).

480 analysed in this study. But, even these optical constants measured on rather similar samples could not
 481 reproduce the reflectance spectra obtained from our laboratory measurements. The simulated reflectance
 482 spectra obtained with the optical constants of their 5%CH₄ tholins show a steeper red slope in the visible,
 483 which is also shifted towards lower wavelengths compared to our laboratory measurements. On the other
 484 hand, the slope of their 1% CH₄ tholins is much weaker. Moreover, the reflectance level of our Pluto
 485 tholins is much higher in the near-infrared. It must however be stressed out that the synthesis process was
 486 significantly different between our Pluto tholins (powder material synthesised while in suspension in the
 487 plasma discharge, see Section 3.1) and the Titan tholins analysed in the above-mentioned studies (organic
 488 films deposited on various substrates).

489 On the contrary, optical constants presented in Khare et al. (1984) reproduce the 5%CH₄ tholins' visible
 490 spectral slope and very near-infrared photometric level reasonably well (see Figure 9). These optical con-
 491 stants are the most commonly used, but they have a poor spectral resolution. Despite the relatively good
 492 fit in the 0.4-1.3 μm range, the four absorption bands observed above 1.3 μm in our laboratory spectra do
 493 not appear in the simulated spectra obtained with the optical constants found in Khare et al. (1984).

494 5.5. Retrieving single scattering albedo from reflectance measurements

495 The previous analysis of existing sets of optical constants clearly showed that it is not possible to repro-
 496 duce our laboratory reflectance measurements from optical constants found in the literature. Consequently,
 497 the single scattering albedo of the Pluto tholins needs to be determined in a different way. It is possible to
 498 isolate and estimate it from the many reflectance spectra collected under various geometries. Indeed, the
 499 phase function $P(g, \lambda)$ and the single scattering albedo $\omega(\lambda)$ are the only unknowns in the simplified Hapke
 500 model formulation given by Equation 1.

501 While the single scattering albedo depends on the wavelength only, the phase function P depends on
 502 both the wavelength and the phase angle g . The wavelength-dependency of the phase function is however
 503 relatively weak (Hapke, 1993, 2012a) and was thus neglected in this analysis. The single scattering albedo
 504 therefore accounts for the full spectral information, while the phase function $P(g)$ is a function of the
 505 illumination and observation geometries only.

506 The laboratory reflectance measurements collected under different illumination and observation condi-
 507 tions, and over a wide spectral range, were all combined together. A non-linear least-squares inversion of
 508 the simplified Hapke model was then applied to retrieve the functions $\omega(\lambda)$ and $P(g)$. There was no more
 509 correlation between the single scattering albedo and the phase function, and therefore they could be esti-
 510 mated simultaneously. Because the reflectance model is highly non-linear, the inversion required an iterative
 511 process, converging towards a unique solution by successive differential corrections from a given initial

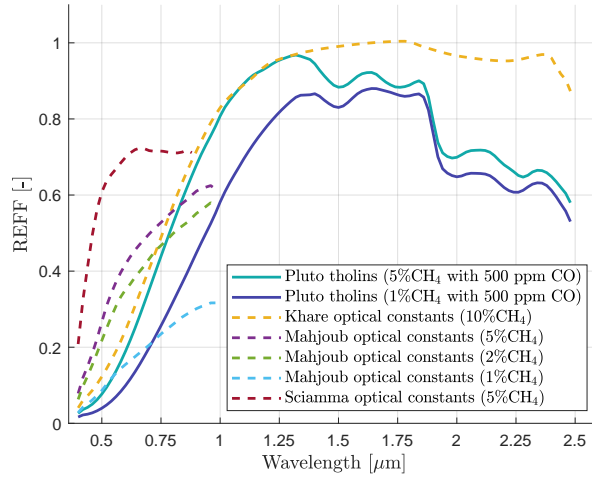


Figure 9: Reflectance calculated from various optical constants to try matching the laboratory measurements (simplified Hapke model as given in Equation 1, with $i = 0^\circ$, $e = 30^\circ$, $g = 30^\circ$, $D = 400$ nm, $P = 1$, $K = 1$).

512 guess. Some convergence issues were first encountered because of the intrinsic constraints of the single scat-
 513 tering albedo values (ranging from 0 to 1). A numerical singularity indeed exists when ω tends towards its
 514 maximum value, and deteriorates the convergence of the least-squares algorithm. An extended grid search
 515 simulation was thus run to identify a good initial guess to initiate the least-square algorithm. More details
 516 about the numerical procedure for the inversion of the Hapke model are provided in Appendix A.1.

517 The results of the Hapke's model inversion are presented in Figures 10 and 11. The consistency between
 518 the grid-search and least-squares solutions for the single scattering albedo is a good indicator of the con-
 519 vergence of the inversion. The solutions obtained for the phase function for both the 5%CH₄ and 1%CH₄
 520 tholins are also insightful. While the phase functions generated by the grid-search analysis are different for
 521 the two tholins, the converged least-squares solutions are conversely extremely similar (see Figure 11). Such
 522 significant differences between the phase functions of the two types of tholins obtained from the grid-search
 523 analysis solutions are not expected, clearly showing the limitations of the initial guess provided by the
 524 grid-search. The results on the phase function also highlight the good convergence of the hybrid inversion
 525 technique and demonstrate the improvement brought by the least-squares algorithm compared to the coarse
 526 grid-search solution.

527 The single scattering albedo of Pluto tholins exhibits a very steep red slope in the visible, which seems
 528 consistent with the New Horizons observations collected over the dark-red terrains of Pluto. In the near-
 529 infrared, ω is very close to 1, in agreement with our laboratory reflectance spectra which show tholins as
 530 extremely bright in the near-infrared. It also explains the difficulties encountered by the simple least-squares
 531 algorithm to converge to an unique solution so close to the numerical singularity if not combined with a
 532 prior grid search analysis.

533 Furthermore, most of the spectral information seems to be captured by the inverted single scattering
 534 albedo. This also proves that the inversion was successful, since ω was the only parameter assumed to be
 535 wavelength-dependent. The four absorption bands identified in our laboratory spectra are indeed present
 536 in the inverted single scattering albedo. Finally, the phase function is globally decreasing with increasing
 537 phase angle. This finding is in agreement with the strong backscattering observed in Figure 7. For both
 538 the 1%CH₄ and 5%CH₄ tholins, the inverted single scattering albedo values are reported in Table A.1 (as
 539 a function of the wavelength) and the phase functions can be found in Table A.2 (see Appendix A.3).

540 6. Comparison with MVIC/LEISA observations

541 Using Pluto tholins' reflectance properties as described in Section 5, their relevance as analogues for the
 542 dark red material covering Cthulhu region was assessed by comparing their reflectance spectra with the New

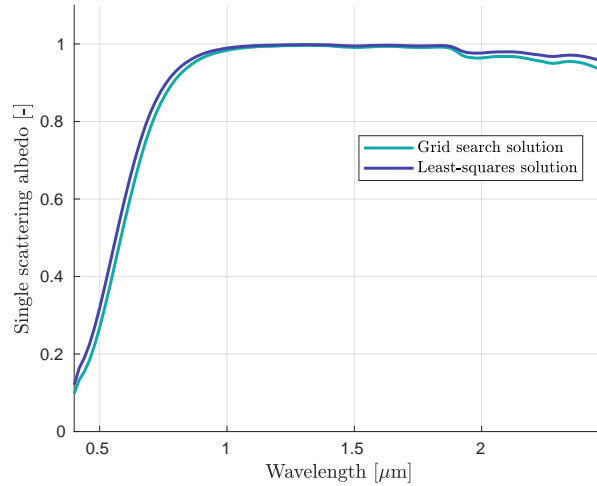


Figure 10: Single Scattering Albedo $\omega(\lambda)$ after inversion of the Hapke model, for 5%CH₄ tholins. The Monte-Carlo solution (displayed in light blue) is still an unconverged solution, only used as an initial guess for the linearised least-squares iterative process

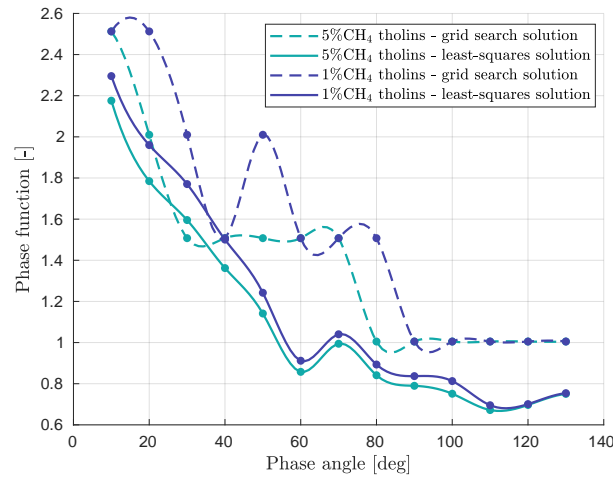


Figure 11: Phase function $P(g)$ after inversion of the Hapke model, for both 5%CH₄ and 1%CH₄ tholins.

543 Horizons data collected by the Ralph instrument when flying over Cthulhu.

544 6.1. Direct comparison of laboratory and New Horizons data

545 6.1.1. Reflectance spectra

546 Before trying to reproduce the New Horizons data using numerical models exposed in Section 4, Cthulhu
 547 spectra were directly compared with laboratory reflectance measurements of Pluto tholins. The comparison
 548 was performed at identical illumination and observation geometries, to prevent any bias in the photometric
 549 level caused by a difference in the measurement geometries. The laboratory spectra were convolved to
 550 match the spectral resolution of the New Horizons observations, which in turn were corrected to account for
 551 photometric calibration issues.

552 Figure 12 shows the superposition of Cthulhu reflectance spectra with those of the pure tholins samples,
 553 under the same geometry. Despite a good agreement at first order for the 1%CH₄ tholins, there are striking
 554 differences between tholins' and New Horizons' spectra, both spectrally and photometrically. The four

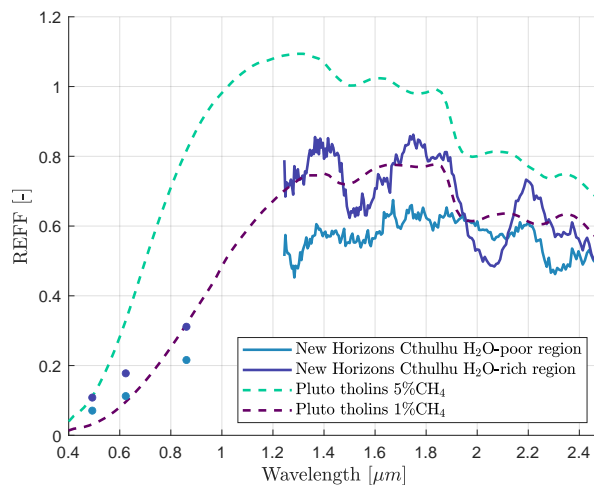


Figure 12: Direct comparison between New Horizons spectra (H₂O-poor and H₂O-rich regions) and laboratory reflectance measurements of 5%CH₄ and 1%CH₄ tholins (under same illumination and observation geometry).

555 absorption bands in tholins laboratory spectra (at 1.5, 1.75, 2.0 and 2.3 μm) are completely absent in the
 556 New Horizons spectra, and the same holds for the spectral features observed in New Horizons data which
 557 do not appear in the tholins spectra.

558 In addition, Figure 12 clearly highlights the influence of the tholins composition. In the near-infrared,
 559 the reflectance of 1%CH₄ tholins is much closer to New Horizons spectra in terms of photometry (being
 560 about 20% lower than that of 5%CH₄ tholins on average). The red slope displayed by the 1%CH₄ tholins
 561 in the visible is also more consistent with MVIC data.

562 6.1.2. Absorption bands in laboratory reflectance spectra

563 The reflectance spectra of the tholins show several absorption features in the near-infrared, as displayed
 564 in Figure 13. As mentioned above, four bands clearly appear in the laboratory measurements at about 1.5
 565 μm , 1.75 μm , 2.0 μm and 2.3 μm .

566 Additional reflectance measurements were conducted on CO-depleted N₂:CH₄ tholins to quantify how the
 567 presence of a small amount of CO in the initial gas mixture affects the tholins spectro-photometric properties.
 568 The result of this comparative analysis is displayed in Figure 14, but no significant spectral difference **and/or**
 569 **band shift** can be observed between the tholins with and without CO. The small difference in photometric
 570 level can be at least partly attributed to slightly different properties of the samples (grain sizes, density,
 571 compaction, *etc.*). These results indicate that the presence of CO is not responsible for any additional
 572 spectral signature in the tholins reflectance spectra. The absorption bands observed in tholins spectra are
 573 thus more likely due to bonds between C, H and N compounds rather than to bonds involving oxygen.

574 The band around 1.75 μm appears to be deeper and wider for 5%CH₄ than for 1%CH₄ tholins. It can
 575 be assigned to the first overtone of the [C-H] bond (Workman, 1996). This is in agreement with the fact
 576 that 5%CH₄ tholins are expected to contain more [C-H] bonds, explaining the stronger absorption of this
 577 feature for 5%CH₄ compared to 1%CH₄ tholins.

578 The absorption feature around 2.25-2.3 μm is thought to be related to the first overtone of the stretching
 579 mode of [C \equiv N] bonds, as proposed in Cruikshank et al. (1991). Another possible interpretation for this
 580 band was proposed by Cloutis (1989), assigning it to combination of aromatic carbon stretch with [C-H]
 581 stretching modes, and combinations of [C-H] stretching and bending modes. However, the shape and depth
 582 of this band does not seem to strongly depend on the N₂/CH₄ ratio of the initial gas mixture from which
 583 the tholins are synthesised, on the contrary to what has been observed for the 1.75 μm band. The fact that
 584 this 1.75 μm absorption feature conserves its shape, width and depth in the reflectance spectra of the two
 585 types of tholins thus appears more consistent with its assignment to [C \equiv N] bonds rather than to [C=C] and

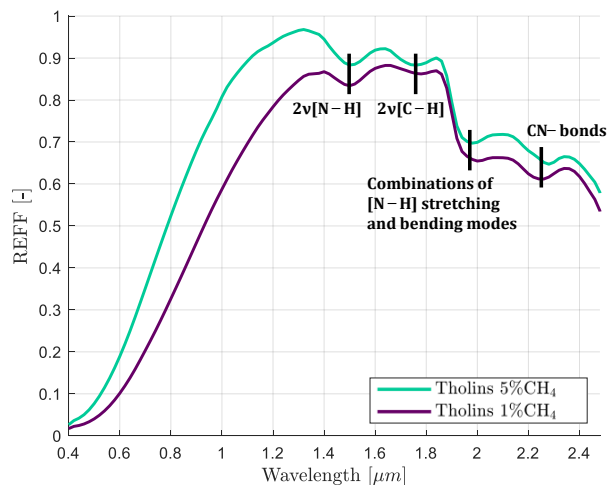


Figure 13: Bands assignment for laboratory reflectance spectra of 5%CH₄ and 1%CH₄ tholins (geometry: $i = 0^\circ$, $e = 30^\circ$).

[C-H] combinations.

The two remaining bands, located around 1.5 μm and 2.0 μm respectively, could at prima facie correspond to H₂O absorption features. However, as mentioned in Section 3.2, additional laboratory reflectance measurements were conducted under vacuum and after heating to verify that adsorbed water was not responsible for any absorption band. The 1.5 μm band is thus more likely related to the first stretching overtone of [N-H] bonds, while the 2.0 μm band can be due to some combinations of [N-H] bending and stretching modes (Workman, 1996). Nevertheless, it must be noted that the presence of those amine functions could be partially related to the synthesis experimental setup, as the formation of nitrogen-bearing compounds is enhanced by wall effects.

The assignment of some tholins' near-infrared absorption bands to [C-H] and [N-H] functions is consistent with previous findings showing that these functions contribute to N₂:CH₄ tholins' mid-infrared spectra (Quirico et al., 2008; Gautier et al., 2012).

6.1.3. Absorption bands in New Horizons spectra

The New Horizons spectra show two main absorption features (see Figures 1 or 12). The first one is located around 2.1 μm . When getting closer to Cthulhu periphery where water ice exists in larger quantities, the H₂O band is contributing to this absorption feature. However, this band still appears in the centre of Cthulhu (*i.e.* in the reddest terrains of Pluto), where very little water ice is expected (as other H₂O absorption bands are not present there). The interpretation of this band is still not firmly resolved (Schmitt et al., 2017).

In addition, another absorption feature is observed around 2.3 μm in the Cthulhu region. Its presence is however thought to be related not to the dark organic material itself, but rather to some hydrocarbon ices with which the red material is expected to be mixed (Cook et al., 2019). Oddly, the shape and depth of this band remain unchanged from Cthulhu's centre to its periphery. The presence of more water ice on the borders of Cthulhu would suggest that the red material is more diluted in water ice there, and more concentrated in Cthulhu's centred, reddest parts. The fact that the 2.3 μm band seems independent of the relative amounts of dark material and water ice favours the assignment of this band to hydrocarbon ices, as suggested in Cook et al. (2019). Furthermore, both Cthulhu spectra exhibit two additional weaker bands at about 1.3-1.35 μm and 1.8-1.85 μm , which might also be linked to these hydrocarbon ices. Figure 15 shows near-infrared spectra of possible hydrocarbon-ices candidates C₂H₆, C₃H₈ and CH₃OH, superimposed upon New Horizons Cthulhu spectra.

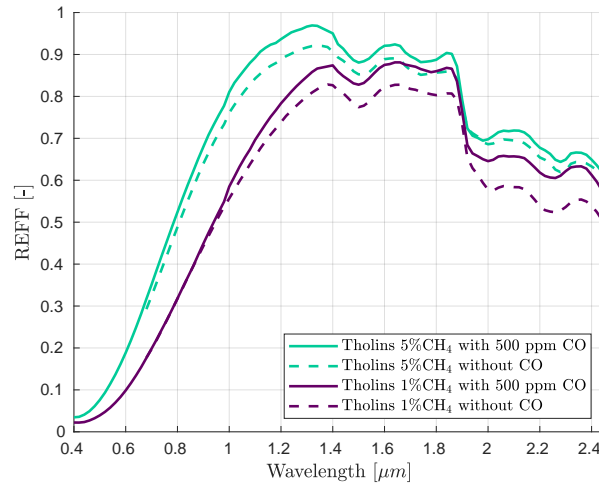


Figure 14: Comparative reflectance measurements of tholins with and without CO: 5%CH₄ (or 1%CH₄) tholins without CO compared to 5%CH₄ (or 1%CH₄) tholins with 500 ppm CO (for CO-depleted tholins, measurements were only conducted from $\lambda = 0.68 \mu\text{m}$).

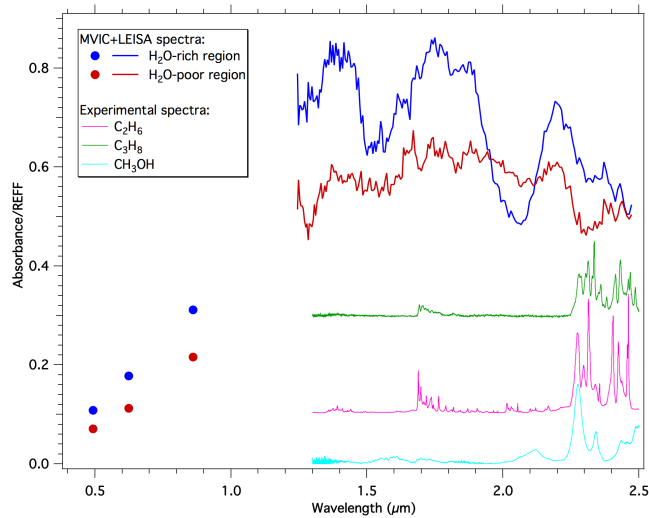


Figure 15: Absorbance spectra of three hydrocarbon ices (C₂H₆, C₃H₈ and CH₃OH) which are potential candidates for the 2.3 μm band observed in Cthulhu's New Horizons near-infrared reflectance spectra (displayed here in blue and red for Cthulhu H₂O-rich and H₂O-poor regions, respectively).

6.2. Optimised fitting between New Horizons data and simulated reflectance

The optimisation process described in Section 4.3 was applied to investigate whether the New Horizons spectra could be reproduced by combining the laboratory reflectance measurements of Pluto tholins (Section 5.2) with the numerical models developed in Sections 4.1 and 4.2.

To account for the diversity of the New Horizons spectra measured over the dark terrains of Pluto, we tried to reproduce the reflectance behaviour of both Cthulhu's H₂O-rich region and H₂O-poor regions, as discussed in Section 2.3. The latter corresponds to the reddest terrains of Pluto and is thus expected to contain the largest relative amounts of the dark Plutonian material.

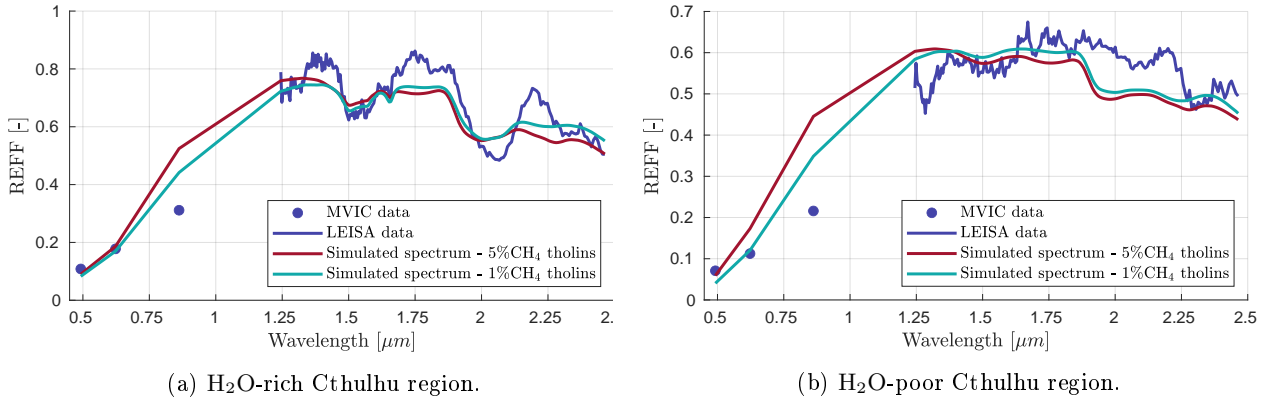


Figure 16: Optimisation results for H₂O-rich region of Cthulhu (left) and H₂O-poor region of Cthulhu (right), using the intimate mixing model described in Section 4.2.2 (*i.e.* spatial mixing between a CH₄-ice unit and an intimate mixing of tholins, H₂O-ice, CH₃OH-ice and C₂H₆-ice). Results are provided for both 5%CH₄ and 1%CH₄ tholins (in red and light blue, respectively).

6.2.1. Intimate mixing between refractory species

The fitting process was first applied to the simple intimate mixing surface model presented in Section 4.2.2. For each species, both the mass fraction in the intimate mixture and particle mean diameter were left as free parameters of the optimisation process, in addition to the macroscopic porosity parameter K . For each set of free parameters, a Hapke model was applied to compute the reflectance of the modelled surface, allowing for a direct comparison with New Horizons spectra.

As shown in Figure 16, the best fits between the modelled surface reflectance and New Horizons spectra were obtained with 1%CH₄ tholins for both H₂O-rich and H₂O-poor terrains of Cthulhu (about 44% and 49% of χ^2 improvement with respect to 5%CH₄ tholins for H₂O-rich and H₂O-poor regions, respectively). This is in agreement with the direct comparison between New Horizons spectra and laboratory reflectance measurements of pure tholins discussed in Section 5.2. As already highlighted, the tholins composition (N₂:CH₄ ratio) has a significant influence on the curvature and steepness of the red slope observed in the visible. Modifying the initial composition of the gas mixture from which the tholins are synthesised might therefore be key when trying to reproduce New Horizons spectra. **The relative amounts of the refractory species which led to the best fits are reported in Table 2, but should be treated cautiously given the poor quality of the fits and the non-uniqueness of the optimisation solution.**

Focusing on H₂O-rich regions first, the simulated reflectance of a mixing between tholins, hydrocarbon and water ices could not accurately reproduce the New Horizons spectrum, even with 1%CH₄ tholins. More precisely, the MVIC point at $\lambda = 0.86 \mu\text{m}$ is not matched and the average reflectance level in the near-infrared of the simulated spectrum is lower than for LEISA spectrum. In particular, this yields a poor fit over the following spectral intervals: 1.3-1.5 μm , 1.65-1.9 μm , and 2.1-2.3 μm , as shown in Figure 16a. The H₂O band at 2.0-2.1 μm is also poorly reproduced.

The weighted MVIC data in the visible provide tight constraints on the required tholins ratio. It thus indirectly drives the average reflectance level in the near-infrared. Although the strong H₂O bands in the near-infrared helps the fitting process by constraining the relative amount of water ice required, the optimisation algorithm fails to reconcile the MVIC data points with high reflectance in the near-infrared.

The fit between the Hapke model and the New Horizons spectrum is significantly worse for the core, H₂O depleted regions of Cthulhu (see Figure 16b). Strong tholins' overtone/combination bands are present in the near-infrared, while they did not appear in the H₂O-rich spectrum due to the presence of clear H₂O bands. To reproduce the averaged spectrum collected over H₂O-poor regions of Cthulhu, H₂O-ice is indeed no longer needed, but matching MVIC data points requires a significant amount of tholins.

This induces a drop in reflectance around $\lambda = 1.9 \mu\text{m}$, consistent with the pure tholins spectra (see Figure 12). Around 1.9 μm , the reflectance of the modelled surface thus becomes much lower than for the

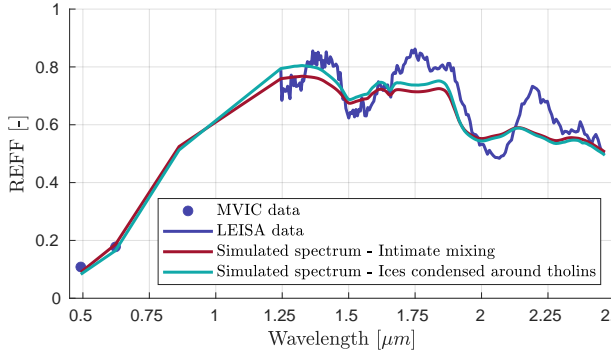
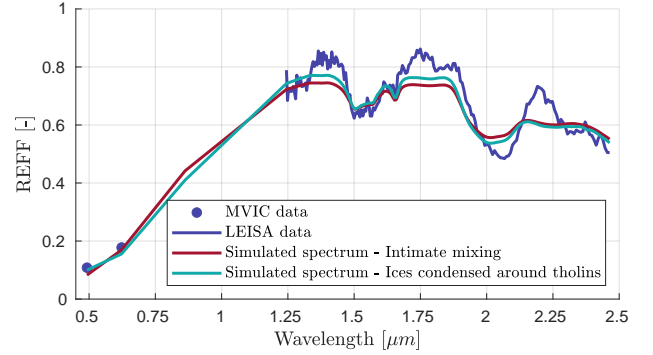
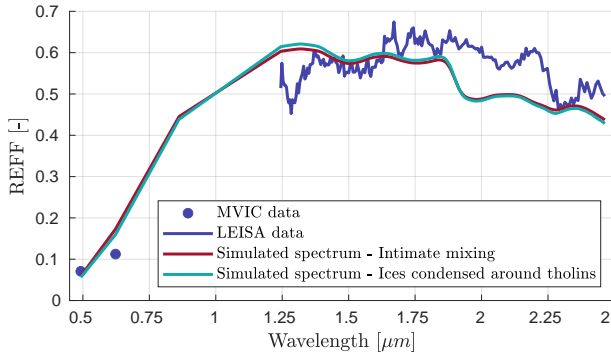
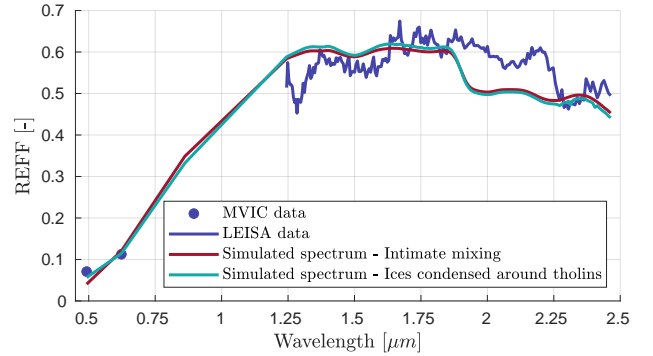

 (a) H₂O-rich Cthulhu region - 5%CH₄ tholins.

 (b) H₂O-rich Cthulhu region - 1%CH₄ tholins.

 (c) H₂O-poor Cthulhu region - 5%CH₄ tholins.

 (d) H₂O-poor Cthulhu region - 1%CH₄ tholins.

Figure 17: Optimisation results for H₂O-rich regions of Cthulhu (upper panel) and H₂O-poor regions of Cthulhu (lower panel), obtained with the two different surface models described in Sections 4.2.2 and 4.2.3: intimate mixing of all refractory species (in red) vs. intimate mixing of ices condensed around core tholins (in light blue). The two types of Pluto tholins were tested with this surface model (5%CH₄ for the top sub-figures and 1%CH₄ for the bottom sub-figures).

657 New Horizons spectrum. In that spectral range, adding more ices to the model would only decrease the
 658 reflectance level further because of the hydrocarbon ices absorption bands. Consequently, the optimisation
 659 process failed not only to remove the tholins bands which are clearly absent in New Horizons data, but also
 660 to reproduce the 2.1 μm and 2.3 μm New Horizons absorption bands (see Section 6.1.3).

661 In the visible, the difference in the spectral slope is larger at $\lambda = 0.49 \mu\text{m}$, but slightly slower at $\lambda =$
 662 $0.86 \mu\text{m}$, compared to the H₂O-rich region case.

663 It must be noted that scaling the MVIC data down or up by 7% (in agreement with the estimated
 664 calibration uncertainty, see Section 2.2) did not yield any noticeable change in the fit between the modelled
 665 spectra and New Horizons data.

666 6.2.2. Ices condensed on tholins particles

667 With the second surface model described in Section 4.2.3, the fraction of core tholins embedded in the
 668 surrounding ice matrix for each icy particle was added to the list of free parameters (already including the
 669 mass ratios of each component of the intimate mixing, as well as their respective mean diameters). The best
 670 fits obtained by the optimiser with this second surface model are provided in Figure 17.

671 Figure 17 compares the fits obtained with the two different surface models (intimate mixing in red, ices
 672 condensed around tholins in light blue), for H₂O-rich and H₂O-poor Cthulhu regions and with both 5%CH₄
 673 and 1%CH₄ tholins. While no significant difference is noticeable between the two surface models for the
 674 H₂O-poor region case, modelling ices as condensed around core tholins yields a slightly better fit for H₂O-rich
 675 regions (about 10% and 34% of χ^2 reduction for 5%CH₄ and 1%CH₄ tholins, respectively). However, this
 676 limited improvement is to be put in perspective as the discrepancies between New Horizons data and the

677 modelled reflectance spectra remain significant regardless of which model is used, especially for H₂O-poor
678 regions. It is thus difficult to conclude about how realistic one surface model is compared to another.

679 Similar conclusions can overall be drawn from the optimisation results, compared to those obtained with
680 the intimate mixing surface model (Section 6.2.1). 1%CH₄ tholins again performed better in reproducing
681 New Horizons data than 5%CH₄ tholins (see Figure 17). They overall led to an improved fit, especially
682 being closer to MVIC data in the visible and matching the photometric level better in the near-infrared.
683 The relative mass ratios of the different refractory species corresponding to the best fits for this second
684 surface model are also provided in Table 2.

685 The reflectance of the H₂O-rich region of Cthulhu is again reasonably well reproduced (see Figures 17a
686 and 17b). However, the simulated spectrum still displays strong tholins absorption bands when little water
687 ice is required while they do not appear in LEISA data (*i.e.* over H₂O-poor Cthulhu regions, see Figures
688 17c and 17d). Moreover, the misfit between the modelled spectra in the visible and MVIC data is far from
689 being fully resolved by using this different surface model, for the point at $\lambda = 0.86 \mu\text{m}$ in particular.

690 It is interesting to note that when using the Maxwell-Garnett model to compute the optical constants
691 of ices condensed around tholins particles, the method selected to derive the value of n does not have
692 any significant effect. As detailed in Section 4.2.3, the method chosen in this work is to use the n values
693 provided in Khare et al. (1984) and compute the values of k which match the single scattering albedo of
694 our laboratory-synthesised tholins. However, the optimisation process was also conducted with a second
695 set of optical constants for the tholins, obtained by assuming n remains constant over the spectral range of
696 interest. No noticeable difference was observed between the results achieved with the two separate sets of
697 tholins optical constants.

	Intimate mixing model		Ices condensed around tholins	
	Species	Mass ratio [%]	Ices	Mass ratio [%]
H₂O-RICH REGION	H ₂ O	88.01	H ₂ O	99.92
	C ₂ H ₆	0.24	C ₂ H ₆	0.04
	CH ₃ OH	0.05	CH ₃ OH	0.04
	1%CH ₄ tholins	11.70		
			Core particles	Fraction embedded material [%]
		1%CH ₄ tholins	18.50	
	Intimate mixing model		Ices condensed around tholins	
	Species	Mass ratio [%]	Ices	Mass ratio [%]
H₂O-POOR REGION	H ₂ O	0.04	H ₂ O	80.81
	C ₂ H ₆	0.08	C ₂ H ₆	16.97
	CH ₃ OH	0.02	CH ₃ OH	2.22
	1%CH ₄ tholins	99.86		
			Core particles	Fraction embedded material [%]
		1%CH ₄ tholins	79.42	

Table 2: Relative amounts of materials which led to the best fits between the reflectance model and New Horizons spectra, when using 1%CH₄ tholins as an analogue for Cthulhu's dark-red material. The values reported in this table are the mass ratios of all refractory species within the first surface unit (*i.e.* refractory unit, see Sections 4.2.2 and 4.2.3) and are given in percentage. Results are provided for the two different surface models and for both H₂O-rich and poor regions. It must be noted that these values must be considered extremely carefully, because of both the non-uniqueness of the solution and poor quality of the fits.

698 7. Discussion

699 Because of the remaining discrepancies between the modelled surface spectra and New Horizons data
700 (see Section 6.2), we cannot yet draw any firm conclusion about the surface's composition and properties in
701 Cthulhu region, and in particular about the exact chemical nature of the red material. Reliable information
702 about the surface can indeed only be derived from Hapke model's parameters when both the photometric
703 level and spectral features are properly fitted.

704 Especially, as previously highlighted, the simulated spectra for H₂O-poor terrains still display tholins

705 absorption features which are absent in LEISA observations. Assuming that the presence of these features is
 706 not only due to experimental limitations discussed in Section 6.1.2, three possible explanations are discussed
 707 here.

708 The terrains may be contaminated by interplanetary dust, bringing dark material into the aerosol layer.
 709 However, to completely attenuate the tholins bands and thus explain their absence in New Horizons spectra,
 710 a significant fraction of darkening material would be needed, which would lead to a severe drop in reflectance
 711 (see results presented in Section 5.3). This seems rather inconsistent with the high reflectance observed in
 712 the near-infrared in LEISA data. We still tried to reproduce New Horizons spectra using darkened tholins
 713 mixed with water and hydrocarbon ices. However, the fit between the modelled surface and the spectra
 714 collected by the MVIC and LEISA instruments was worse than the one obtained with pure tholins samples
 715 (figures are not shown as the extremely poor quality of the fit does not convey any valuable information).
 716 The absence of absorption features thus cannot be explained by interplanetary dust contamination of the
 717 red material, as the drop in reflectance it would induce in the near-infrared was shown to be incompatible
 718 with the high photometric level measured by LEISA over the Cthulhu region.

719 As a second hypothesis, Galactic Cosmic Rays (GCR) irradiation is known to promote dehydrogenation
 720 reactions, formation of unsaturated bonds (olefinic or acetylenic), cross-linking and disorder (Balanzat et al.,
 721 1995). This phenomenon could explain the darkening of tholins and the attenuation of their absorption
 722 features, and might therefore justify the absence of absorption bands in New Horizons spectra. **This would
 723 likely affect the photometric level in the near-infrared as well, and not only the spectral contrast.** Radiolysis
 724 could also have an effect on the shape of the spectral slope in the visible through the production of conjugated
 725 unsaturated carbons, which might **alter** the current fit of the spectral slope for the H₂O-poor terrains of
 726 Cthulhu. The irradiation dose for a tholins grain on the surface of Pluto can be estimated using the proton
 727 flux of Webber and Yushak (1983), assuming the contribution of heavier ions by scaling the proton flux
 728 density with their cosmic abundance (Meyer et al., 1998). Here, it is assumed that the GCR density flux
 729 is that of local Interstellar Medium, neglecting heliospheric shielding. We also neglect the energy loss
 730 of the incoming ions in Pluto's atmosphere. This estimate is therefore an upper value. The electronic and
 731 nuclear stopping powers, S_e and S_n , respectively, were calculated with the SRIM software for a H:C:N=1:1:1
 732 stoichiometry and a tholins density $\rho = 1 \text{ g.cm}^{-3}$ (Ziegler and Manoyan, 1988). The dose can then be written
 733 as

$$\begin{aligned} \text{Dose[eV.at}^{-1}]_{e,n} & \hspace{15em} (13) \\ & = \Delta t \frac{4\pi M}{\rho N_A} \sum_{Z=1}^{92} \int_{E_{min}}^{E_{max}} A(Z) \frac{dN}{dE} S_{e,n}^Z dE, \end{aligned}$$

734 where M is the molar mass, N_A the Avogadro number, E_{min} and E_{max} the edges of the energy range,
 735 $\frac{dN}{dE}$ the proton flux density from Webber and Yushak (1983), $A(Z)$ the relative abundance of element Z
 736 relative to hydrogen and Δt is the irradiation time.

737 The irradiation time of a given grain in the aerosol layer depends on the deposition rate and the pen-
 738 etration depth of ions, which is controlled by its mass and energy. Figure 18 reports the GCR density
 739 flux plotted versus the penetration depth for H and Fe ions, which are the lightest and heaviest abundant
 740 ions that contribute to the deposited dose. In the case of protons, 99% of GCR energy is deposited within
 741 0-24 m. **The aerosol layer (roughly estimated to be of the order of 10 m,** Grundy et al., 2018) was then
 742 totally irradiated during 4.55 Gyrs, but a given grain within this layer received a varying dose due to the
 743 continuous aerosol deposition. In contrast, the iron ions deliver 99 % of GCR energy in the range 0-0.48 m,
 744 which corresponds roughly to an aerosol deposition duration of 140 Myrs.

745 The probing depth of visible and near-infrared photons can be estimated to 1 mm, as the mean optical
 746 path length calculated from Hapke theory (Clark and Roush, 1984). This depth corresponds to an irradiation
 747 time of 280000 years with the sedimentation rate of Grundy et al. (2018). This leads to upper values of
 748 the electronic and nuclear doses deposited in this thin layer of $2.4 \times 10^{-2} \text{ eV.atom}^{-1}$ and $10^{-5} \text{ eV.atom}^{-1}$,
 749 respectively. The electronic dose is small and may lead to weak or moderate chemical and structural
 750 changes, according to previous studies on polymers degradation (*e.g.* Balanzat et al., 1995; Faure et al.,

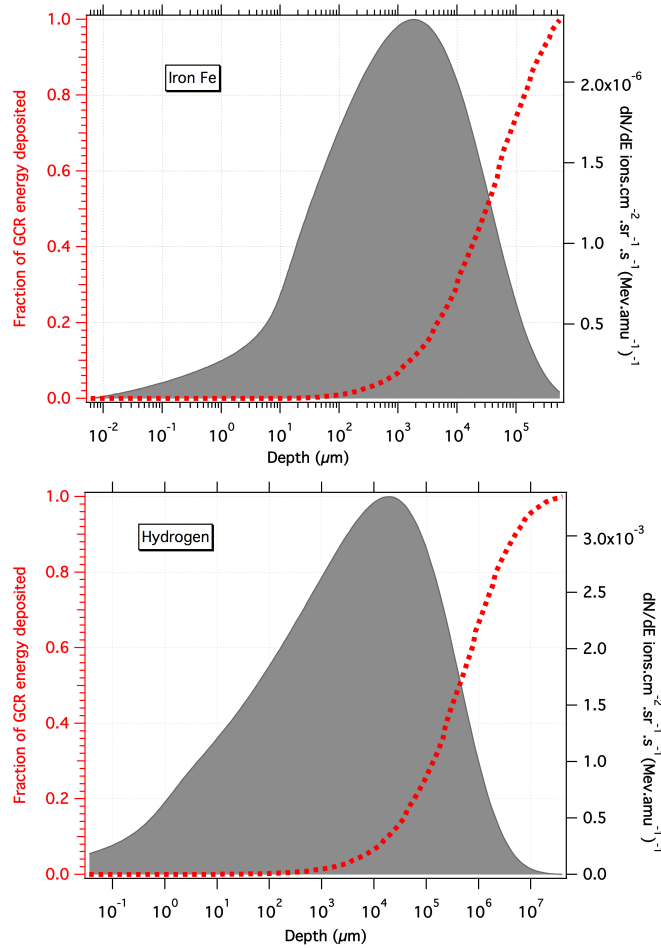


Figure 18: GCR flux density and fraction of GCR flux density deposited in the aerosol layer plotted against the penetration depth for Iron (top) and Hydrogen (bottom).

751 2021). Therefore, we expect a limited effect on the chemical and optical properties of aerosols. However,
 752 these results need to be confirmed by dedicated irradiation experiments on tholins.

753 Finally, a high porosity of the dark terrains is another possible explanation for the lack of strong ab-
 754 sorption features caused by the dark material in New Horizons data. Laboratory experiments showed that a
 755 highly porous tholins crust, formed from sublimation experiments, does not display combination / overtone
 756 bands in the near-infrared (Poch et al., 2016). **It must be stressed that such micro-porosity effects are by
 757 definition not accounted for by the macroscopic porosity parameter K in Hapke model, and are thus not
 758 included in our work.** Figure 19 reports the reflectance spectra of a mixture of water-ice, olivine, $\text{N}_2:\text{CH}_4 =$
 759 95%:5% tholins (without CO) and smectite, collected before and after sublimation and presented in Poch
 760 et al. (2016). The reflectance of our Pluto tholins is displayed as well, and the absence of any remarkable
 761 spectral feature in the post-sublimation measurements is clear (from neither tholins nor any of the other
 762 species).

763 Evidences for N_2 and CH_4 sublimation cycles on Pluto's surface were described in Schmitt et al. (2017);
 764 Bertrand et al. (2018, 2019), but these sublimation cycles do not appear to involve Cthulhu region. This
 765 region is actually supposed to be depleted of N_2 -ice (N_2 being too volatile to subsist in these hot, low albedo
 766 areas). Moreover, the very small amounts of CH_4 detected in Cthulhu are mainly located on mountains
 767 (Bertrand et al., 2020), while there is no spectral evidence for CH_4 in the reddest, H_2O -poor Cthulhu
 768 terrains. Only a very thin CH_4 condensation layer may occur during night (Bertrand et al., 2020).

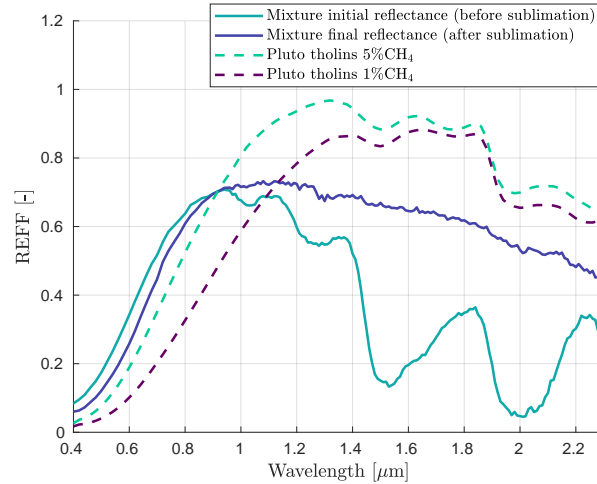


Figure 19: Reflectance spectra of our two Pluto tholins, superimposed with results of a sublimation experiment from Poch et al. (2016): a mixture of water-ice with olivine (1%), $N_2:CH_4 = 95\%:5\%$ tholins (0.5%) and smectite (0.1%) underwent sublimation at low temperature (-70°C) and pressure ($1\text{-}2\cdot 10^{-5}$ mbar). The reflectance spectra of this mixture are displayed before sublimation, and about 40 h afterwards, after formation of a sublimation mantle on top of the sample (see Figure 5e in Poch et al. (2016)).

769 However, the lack of strong evidence for CH_4 sublimation cycles in Cthulhu region after New Horizons'
 770 flyby does not completely rule out the possibility of this region being covered by CH_4 frosts during other
 771 seasons or obliquity periods. Even without sublimation cycles, deposition of light aerosols at very low tem-
 772 perature and under the weak gravity acting on Pluto could anyway promote the formation of highly porous
 773 surfaces, which do not show bands in the near-infrared. Again, this hypothesis requires further investiga-
 774 tion. Simulating porous surfaces via sublimation of a Pluto tholins/ice mixture or via gentle sedimentation
 775 of Pluto tholins at low temperature would be an interesting future step, in order to assess how the porosity
 776 affects their reflectance spectrum.

777 8. Conclusions

778 Different hypotheses still coexist to explain the origin and composition of the non-icy, reddish material
 779 covering Pluto's dark terrains. They include irradiation of the surface ices (Cruikshank et al., 2015), as well
 780 as formation of complex, macromolecular organic compounds in a warm liquid ocean created by the giant
 781 impact which formed both Pluto and Charon (Sekine et al., 2017). It has also been suggested that Pluto's
 782 dark material could consist of deposited aerosols originating from the dissociation and ionisation of Pluto's
 783 atmospheric gases (*e.g.* Cheng et al., 2017; Grundy et al., 2018). This would be in agreement with the recent
 784 findings exposed in Protopapa et al. (2020) according to which a single colouring agent could explain the
 785 whole diversity of Pluto's surface colours. In this perspective, this study led to a better characterisation
 786 of the reflectance properties of two types of Pluto tholins, to assess their relevance as plausible aerosols
 787 analogues for the yet unidentified reddish material covering Cthulhu region.

788 The reflectance spectra of these tholins were collected under various illumination and observation geome-
 789 tries, highlighting a strong backscattering behaviour. We then numerically retrieved Pluto tholins' single
 790 scattering albedo and phase function from their reflectance measurements, by inverting a simplified Hapke
 791 model. Feeding these optical properties into a simplified Hapke reflectance model, an optimisation process
 792 was set up to assess whether it is possible to reproduce New Horizons spectra with our reflectance model
 793 while using Pluto tholins as analogues for the dark material. A mix of tholins and CH_4 , H_2O , CH_3OH , and
 794 C_2H_6 ices was assumed and two different surface models were tested (intimate mixing between all refractory
 795 species and condensation of icy species around core tholins particles, respectively).

796 $1\%CH_4$ tholins overall led to significantly better fits than $5\%CH_4$ tholins. Especially, they better match

797 the MVIC data in the visible and the average photometric level in the near-infrared. This indicates that
 798 slightly changing the composition of our Pluto tholins might improve the fit with respect to New Horizons
 799 data. Still, our optimisation algorithm failed to fit the three MVIC data points perfectly, even with 1%CH₄
 800 tholins. This misfit in the visible needs to be investigated further, especially since reproducing the strong
 801 red slope that Cthulhu's spectra exhibit is key to unravel the composition and origin of the dark red material
 802 covering this region of Pluto.

803 New Horizons data collected over the H₂O-rich region of Cthulhu are easier to reproduce with our surface
 804 reflectance model than H₂O-poor region' spectra. The strong H₂O absorption bands dominate the near-
 805 infrared part of the H₂O-rich region' spectrum and hide the absorption bands clearly visible in the tholins
 806 spectra. On the other hand, the four absorption features of Pluto tholins appear in the simulated spectra
 807 of H₂O-poor region, while they are absent in New Horizons data.

808 The presence of the tholins bands in the modelled spectra prevented the optimisation algorithm from
 809 reproducing the near-infrared features of the New Horizons spectrum. It is therefore crucial to understand
 810 which phenomena could explain such an attenuation of the spectral contrast before concluding about how
 811 representative tholins are of the dark red organic material on Pluto. The possible supply in dark material
 812 brought by impacting interplanetary dust particles does not seem to be a very plausible hypothesis, since
 813 mixing tholins with a darkening agent tends to strongly decrease the reflectance level and not only remove
 814 the absorption bands. The effect of GCR irradiation remains to be further investigated, but its contribution
 815 might likely be insufficient. However, the effect of a high porosity in the Cthulhu terrains might provide
 816 an explanation for the lack of strong absorption features in New Horizons spectra, and also requires deeper
 817 analyses.

818 The presence of some of the absorption bands in Pluto tholins' reflectance spectra could also be partially
 819 related to the way they are synthesised. This more precisely concerns the two bands related to amine
 820 functions (*i.e.* 1.5 μm and 2.0 μm bands, see Section 6.1.2). The formation of amine functional groups is
 821 indeed known to be enhanced by wall effect in the PAMPRE experimental setup, which could explain the
 822 intensity of some of the absorption bands. Another point is that the tholins synthesis was conducted at room
 823 temperature, while the formation of haze particles occurs at much lower temperature in Pluto's atmosphere.
 824 To our knowledge, no tholins were collected at low-temperature in cold plasma reactors. Bernard et al.
 825 (2003, 2006) and Brucato et al. (2010) used a cryogenic trap in their experiments to collect volatile species,
 826 but their samples were synthesized at room temperature and cannot be used as low-temperature tholins (as
 827 mentioned in Brasse et al., 2015). Some temperature effects are however expected, such as the condensation
 828 of free molecules that would result in an increase of the soluble organic fraction. Nevertheless, we still expect
 829 the presence of similar functional groups as in tholins synthesised so far and we therefore do not foresee any
 830 significant impact on our conclusions.

831 Finally, all our analysis is based on extremely limited reflectance models, the simplicity of which might
 832 affect our simulated spectra. The isotropic phase function assumption may for instance alter the photometric
 833 level, but also the spectral slope and the band depths. Pluto tholins show a strong backscattering behaviour
 834 (see Section 5.2), while ices are on the contrary characterised by a strong forward-scattering. The variations
 835 of the phase function as a function of both the geometry and the wavelength are thus hard to predict, making
 836 the isotropic assumption a severe limitation of our current model.

837 It must also be stressed that there is no guarantee of the solution's uniqueness when fitting a Hapke
 838 reflectance model to an existing spectrum. Nonetheless, this does not hinder the relevance of our approach
 839 since we are not estimating specific surface properties from our best fit, but are only trying to reproduce
 840 Cthulhu's reflectance using tholins as analogues for Pluto's dark organic material.

841 Finally, the optical properties of our Pluto tholins (including optical constants n and k) were retrieved
 842 from a purely numerical inversion of a highly simplified radiative transfer model, applied on reflectance
 843 measurements performed on a complex medium. However, to rigorously extract optical constants, it is
 844 preferable to use films deposited on plane surfaces, for which simplified optical transmission models are
 845 better-suited (Trotta, 1996). For this reason, the inverted optical constants used in this work and provided
 846 in Appendix A.3 need to be treated cautiously. An additional, similar analysis based on recently determined
 847 optical constants for Pluto tholins might be insightful (Jovanović et al., 2021).

848 **Acknowledgements**

849 This work was supported by NASA's New Horizons Project. M. Fayolle, E. Quirico, B. Schmitt, L.
 850 Gabosova and O. Poch acknowledge the Centre National d'Etudes Spatiales (CNES) for its financial support
 851 through its "Systeme Solaire" program (it is based on observations with RALPH embarked on New Horizons)
 852 and the ANR Project CLASSY. O.P. acknowledges funding from the Centre National d'Etudes Spatiales
 853 (CNES) and the European Research Council under grant SOLARYS (77169). T.G. Thanks CNES and PNP
 854 for their financial support. N.C and L.J thank the European Research Council for funding via the ERC
 855 PrimChem project (grant agreement No. 636829). We would like to thank the two anonymous reviewers
 856 for their careful reading and useful feedback, which significantly contributed to improve the quality of our
 857 manuscript.

858 **References**

- 859 Alcouffe, G., Cavarroc, M., Cernogora, G., Ouni, F., Jolly, A., Boufendi, L., Szopa, C., 2009. Capacitively coupled plasma used
 860 to simulate Titan's atmospheric chemistry. *Plasma Sources Science and Technology* 19, 015008.
- 861 Balanzat, E., Betz, N., Bouffard, S., 1995. Swift heavy ion modification of polymers. *Nuclear Instruments and Methods in*
 862 *Physics Research Section B: Beam Interactions with Materials and Atoms* 105, 46–54.
- 863 Bernard, J.M., Coll, P., Coustenis, A., Raulin, F., 2003. Experimental simulation of Titan's atmosphere: Detection of ammonia
 864 and ethylene oxide. *Planetary and Space Science* 51, 1003–1011.
- 865 Bernard, J.M., Quirico, E., Brissaud, O., Montagnac, G., Reynard, B., McMillan, P., Coll, P., Nguyen, M.J., Raulin, F.,
 866 Schmitt, B., 2006. Reflectance spectra and chemical structure of Titan's tholins: Application to the analysis of Cassini-
 867 Huygens observations. *Icarus* 185, 301–307.
- 868 Bertrand, T., Forget, F., Schmitt, B., White, O.L., Grundy, W.M., 2020. Equatorial mountains on Pluto are covered by
 869 methane frosts resulting from a unique atmospheric process. *Nature communications* 11, 1–7.
- 870 Bertrand, T., Forget, F., Umurhan, O., Grundy, W., Schmitt, B., Protopapa, S., Zangari, A., White, O., Schenk, P., Singer,
 871 K., et al., 2018. The nitrogen cycles on Pluto over seasonal and astronomical timescales. *Icarus* 309, 277–296.
- 872 Bertrand, T., Forget, F., Umurhan, O., Moore, J., Young, L., Protopapa, S., Grundy, W., Schmitt, B., Dhingra, R., Binzel, R.,
 873 et al., 2019. The CH₄ cycles on Pluto over seasonal and astronomical timescales. *Icarus* 329, 148–165.
- 874 Brasse, N., Munoz, O., Coll, P., Raulin, F., 2015. Optical constants of Titan aerosols and their tholin analogs: experimental
 875 results and modeling/observational data. *Planetary and Space Science* 109–110, 159–174.
- 876 Brucato, J., Migliorini, A., Barucci, M., Carvano, J., Dotto, E., Mennella, V., 2010. Reflectance spectra of Titan tholin between
 877 7000 and 10 cm⁻¹-Interpretation of Cassini/CIRS observation of Saturn's satellite Phoebe. *Astronomy & Astrophysics* 516,
 878 A92.
- 879 Buie, M.W., Grundy, W.M., Young, E.F., Young, L.A., Stern, S.A., 2010. Pluto and Charon with the Hubble Space Telescope.
 880 I. Monitoring global change and improved surface properties from light curves. *The Astronomical Journal* 139, 1117.
- 881 Buie, M.W., Tholen, D.J., 1989. The surface albedo distribution of Pluto. *Icarus* 79, 23–37.
- 882 Canup, R.M., 2010. On a giant impact origin of Charon, Nix, and Hydra. *The Astronomical Journal* 141, 35.
- 883 Cheng, A.F., Summers, M.E., Gladstone, G.R., Strobel, D.F., Young, L.A., Lavvas, P., Kammer, J.A., Lisse, C.M., Parker,
 884 A.H., Young, E.F., et al., 2017. Haze in Pluto's atmosphere. *Icarus* 290, 112–133.
- 885 Clark, R.N., Roush, T.L., 1984. Reflectance spectroscopy: Quantitative analysis techniques for remote sensing applications.
 886 *Journal of Geophysical Research: Solid Earth* 89, 6329–6340.
- 887 Cloutis, E., 1989. Spectral Reflectance Properties of Hydrocarbons: Remote-Sensing Implications. *Science* 245, 165–168.
- 888 Coll, P., Navarro-González, R., Szopa, C., Poch, O., Ramírez, S.I., Coscia, D., Raulin, F., Cabane, M., Buch, A., Israël, G.,
 889 2013. Can laboratory tholins mimic the chemistry producing Titan's aerosols? A review in light of ACP experimental results.
 890 *Planetary and Space Science* 77, 91–103.
- 891 Cook, J.C., Dalle Ore, C.M., Protopapa, S., Binzel, R.P., Cruikshank, D.P., Earle, A., Grundy, W.M., Ennico, K., Howett, C.,
 892 Jennings, D.E., et al., 2019. The distribution of H₂O, CH₃OH, and hydrocarbon-ices on Pluto: Analysis of New Horizons
 893 spectral images. *Icarus* 331, 148–169.
- 894 Cruikshank, D., Allamandola, L., Hartmann, W., Tholen, D., Brown, R., Matthews, C., Bell, J., 1991. Solid C ≡ N Bearing
 895 Material on Outer Solar System Bodies. *Icarus* 94, 345–353.
- 896 Cruikshank, D., Grundy, W., DeMeo, F., Buie, M., Binzel, R., Jennings, D., Olkin, C., Parker, J., Reuter, D., Spencer, J.,
 897 et al., 2015. The surface compositions of Pluto and Charon. *Icarus* 246, 82–92.
- 898 Cruikshank, D., Pilcher, C., Morrison, D., 1976. Pluto: Evidence for methane frost. *Science*, 835–837.
- 899 Cruikshank, D.P., Mason, R., Dalle Ore, C., Bernstein, M., Quirico, E., Mastrapa, R., Emery, J., Owen, T., 2006. Ethane on
 900 Pluto and Triton, in: *DPS*, pp. 21–03.
- 901 DeMeo, F.E., Dumas, C., de Bergh, C., Protopapa, S., Cruikshank, D.P., Geballe, T.R., Alvarez-Candal, A., Merlin, F.,
 902 Barucci, M.A., 2010. A search for ethane on Pluto and Triton. *Icarus* 208, 412–424.
- 903 Desch, S.J., 2015. Density of Charon formed from a disk generated by the impact of partially differentiated bodies. *Icarus* 246,
 904 37–47.
- 905 Faure, M., Quirico, E., Faure, A., Boduch, P., Rothard, H., Balanzat, E., Baklouti, D., Brunetto, R., Bonal, L., Beck, P.,

- 906 et al., 2021. A radiolytic origin of organic matter in primitive chondrites and trans-neptunian objects? new clues from ion
907 irradiation experiments. *Icarus* , 114462.
- 908 Fayolle, M., Quirico, E., Potin, S., 2018. Bidirectional Vis-NIR reflectance spectra of two tholins samples (+ mixtures with
909 pyrrhotite) at various illumination-observation geometries ($i=0,30,60$ deg - $e=-70$ to 70 deg) and their extracted single
910 scattering albedo and optical constants spectra. SSHADE/GhoSST (OSUG Data Center). dataset/spectral data. URL:
911 doi:10.26302/SSHADE/EXPERIMENT_BS_20201201_001.
- 912 Gao, P., Fan, S., Wong, M.L., Liang, M.C., Shia, R.L., Kammer, J.A., Yung, Y.L., Summers, M.E., Gladstone, G.R., Young,
913 L.A., et al., 2017. Constraints on the microphysics of Pluto's photochemical haze from New Horizons observations. *Icarus*
914 287, 116–123.
- 915 Gautier, T., Carrasco, N., Mahjoub, A., Vinatier, S., Giuliani, A., Szopa, C., Anderson, C.M., Correia, J.J., Dumas, P.,
916 Cernogora, G., 2012. Mid-and far-infrared absorption spectroscopy of Titan's aerosols analogues. *Icarus* 221, 320–327.
- 917 Gladstone, G.R., Stern, S.A., Ennico, K., Olkin, C.B., Weaver, H.A., Young, L.A., Summers, M.E., Strobel, D.F., Hinson,
918 D.P., Kammer, J.A., et al., 2016. The atmosphere of Pluto as observed by New Horizons. *Science* 351.
- 919 Goldberg, D.E., 1989. Genetic algorithms in search. *Optimization, and Machine Learning* .
- 920 Grundy, W., Bertrand, T., Binzel, R., Buie, M., Buratti, B., Cheng, A., Cook, J., Cruikshank, D., Devins, S., Dalle Ore, C.,
921 Earle, A., Ennico, K., Forget, F., Gao, P., Gladstone, G., Howett, C., Jennings, D., Kammer, J., Lauer, T., Linscott, I.,
922 Lisse, C., Lunsford, A., McKinnon, W., Olkin, C., Parker, A., Protopapa, S., Quirico, E., Reuter, D., Schmitt, B., Singer,
923 K., Spencer, J., Stern, S., Strobel, D., Summers, M., Weaver, H., Weigle, G., Wong, M., Young, E., Young, L., Zhang, X.,
924 2018. Pluto's haze as a surface material. *Icarus* 306 , 232–245.
- 925 Grundy, W., Binzel, R., Buratti, B., Cook, J., Cruikshank, D., Dalle Ore, C., Earle, A., Ennico, K., Howett, C., Lunsford, A.,
926 et al., 2016. Surface compositions across Pluto and Charon. *Science* 351.
- 927 Grundy, W., Buie, M., 2002. Spatial and compositional constraints on non-ice components and H₂O on Pluto's surface. *Icarus*
928 157, 128–138.
- 929 Grundy, W., Schmitt, B., Quirico, E., 2002. The temperature-dependent spectrum of methane ice I between 0.7 and 5 μ m and
930 opportunities for near-infrared remote thermometry. *Icarus* 155, 486–496.
- 931 Hadamcik, E., Renard, J.B., Alcouffe, G., Cernogora, G., Lévassieur-Regourd, A.C., Szopa, C., 2009. Laboratory light-scattering
932 measurements with Titan's aerosols analogues produced by a dusty plasma. *Planetary and Space Science* 57, 1631–1641.
- 933 Hapke, B., 1986. Bidirectional Reflectance Spectroscopy: 4. The extinction Coefficient and the Opposition Effect. *Icarus* 67 ,
934 264–280.
- 935 Hapke, B., 1993. *Theory of Reflectance and Emittance Spectroscopy*. Cambridge University Press, Cambridge.
- 936 Hapke, B., 2002. Bidirectional Reflectance Spectroscopy: 5. The Coherent Backscatter Opposition Effect and Anisotropic
937 Scattering. *Icarus* 157 , 523–534.
- 938 Hapke, B., 2008. Bidirectional Reflectance Spectroscopy: 6. Effects of porosity. *Icarus* 198 , 918–926.
- 939 Hapke, B., 2012a. Bidirectional Reflectance Spectroscopy: 7. The single particle phase function hockey stick relation. *Icarus*
940 221 , 1079–1083.
- 941 Hapke, B., 2012b. *Theory of reflectance and emittance spectroscopy*. Cambridge university press.
- 942 Holler, B., Young, L., Grundy, W., Olkin, C., Cook, J., 2014. Evidence for longitudinal variability of ethane ice on the surface
943 of Pluto. *Icarus* 243, 104–110.
- 944 Howett, C., Parker, A., Olkin, C., Reuter, D., Ennico, K., Grundy, W., Graps, A., Harrison, K., Throop, H., Buie, M., et al.,
945 2017. Inflight radiometric calibration of new horizons's multispectral visible imaging camera (mvic). *Icarus* 287, 140–151.
- 946 Jovanović, L., Gautier, T., Broch, L., Protopapa, S., Bertrand, T., Rannou, P., Fayolle, M., Quirico, E., Johann, L., Naciri,
947 A.E., et al., 2021. Optical constants of pluto aerosol analogues from uv to near-ir. *Icarus* 362, 114398.
- 948 Jovanović, L., Gautier, T., Vuitton, V., Wolters, C., Bourgalais, J., Buch, A., Orthous-Daunay, F.R., Vettier, L., Flandinet,
949 L., Carrasco, N., 2020. Chemical composition of Pluto aerosol analogues. *Icarus* , 113774.
- 950 Khare, B., Sagan, C., Arakawa, E., Suits, F., Callcott, T., Williams, M., 1984. Optical Constants of Organic Tholins Produced
951 in a Simulated Titanian Atmosphere: From Soft X-Ray to Microwave Frequencies. *Icarus* 60 , 127–137.
- 952 Lellouch, E., Gurwell, M., Butler, B., Fouchet, T., Lavvas, P., Strobel, D., Sicardy, B., Moullet, A., Moreno, R., Bockelée-
953 Morvan, D., et al., 2017. Detection of CO and HCN in Pluto's atmosphere with ALMA. *Icarus* 286, 289–307.
- 954 Luspay-Kuti, A., Mandt, K., Jessup, K.L., Kammer, J., Hue, V., Hamel, M., Filwett, R., 2017. Photochemistry on Pluto - I.
955 Hydrocarbons and aerosols. *Monthly Notices of the Royal Astronomical Society* 472, 104–117.
- 956 Mahjoub, A., Carrasco, N., Dahoo, P.R., Gautier, T., Szopa, C., Cernogora, G., 2012. Influence of methane concentration on
957 the optical indices of Titan's aerosols analogues. *Icarus* 221 , 670–677.
- 958 McKinnon, W.B., Stern, S., Weaver, H., Nimmo, F., Bierson, C., Grundy, W., Cook, J., Cruikshank, D., Parker, A., Moore,
959 J., et al., 2017. Origin of the Pluto–Charon system: Constraints from the New Horizons flyby. *Icarus* 287, 2–11.
- 960 Meyer, J.P., Drury, L.O., Ellison, D.C., 1998. A cosmic-ray composition controlled by volatility and A/Q ratio. SNR shock
961 acceleration of gas and dust, in: *The Advanced Composition Explorer Mission*. Springer, pp. 179–201.
- 962 Nakamura, R., Sumikawa, S., Ishiguro, M., Mukai, T., Iwamura, F., Terada, H., Motohara, K., Goto, M., Hata, R., Taguchi,
963 T., et al., 2000. Subaru infrared spectroscopy of the Pluto-Charon system. *Publications of the Astronomical Society of*
964 *Japan* 52, 551–556.
- 965 Olkin, C.B., Spencer, J.R., Grundy, W.M., Parker, A.H., Beyer, R.A., Schenk, P.M., Howett, C.J., Stern, S.A., Reuter, D.C.,
966 Weaver, H.A., et al., 2017. The global color of Pluto from New Horizons. *The Astronomical Journal* 154, 258.
- 967 Owen, T.C., Roush, T.L., Cruikshank, D.P., Elliot, J.L., Young, L.A., De Bergh, C., Schmitt, B., Geballe, T.R., Brown, R.H.,
968 Bartholomew, M.J., 1993. Surface ices and the atmospheric composition of Pluto. *Science* 261, 745–748.

- 969 Poch, O., Pommerol, A., Jost, B., Carrasco, N., Szopa, C., Thomas, N., 2016. Sublimation of ice-tholins mixtures: a morpho-
970 logical and spectrophotometric study. *Icarus* 266 , 288–305.
- 971 Potin, S., Brissaud, O., Beck, P., Schmitt, B., Magnard, Y., Correia, J.J., Rabou, P., Jocu, L., 2018. SHADOWS: a spectro-
972 gonio radiometer for bidirectional reflectance studies of dark meteorites and terrestrial analogs: design, calibrations, and
973 performances on challenging surfaces. *Applied optics* 57, 8279–8296.
- 974 Protopapa, S., Boehnhardt, H., Herbst, T., Cruikshank, D., Grundy, W., Merlin, F., Olkin, C., 2008. Surface characterization
975 of Pluto and Charon by L and M band spectra. *Astronomy & Astrophysics* 490, 365–375.
- 976 Protopapa, S., Grundy, W., Reuter, D., Hamilton, D., Dalle Ore, C., Cook, J., Cruikshank, D., Schmitt, B., Philippe, S.,
977 Quirico, E., et al., 2017. Pluto's global surface composition through pixel-by-pixel Hapke modeling of New Horizons
978 Ralph/LEISA data. *Icarus* 287, 218–228.
- 979 Protopapa, S., Olkin, C.B., Grundy, W.M., Li, J.Y., Verbiscer, A., Cruikshank, D.P., Gautier, T., Quirico, E., Cook, J.C.,
980 Reuter, D., et al., 2020. Disk-resolved Photometric Properties of Pluto and the Coloring Materials across its Surface. *The*
981 *Astronomical Journal* 159, 74.
- 982 Quirico, E., Montagnac, G., Lees, V., McMillan, P.F., Szopa, C., Cernogora, G., Rouzaud, J.N., Simon, P., Bernard, J.M.,
983 Coll, P., et al., 2008. New experimental constraints on the composition and structure of tholins. *Icarus* 198, 218–231.
- 984 Quirico, E., Schmitt, B., 1997. Near-Infrared Spectroscopy of Simple Hydrocarbons and Carbon Oxides Diluted in Solid N₂ and
985 as Pure Ices: Implications for Triton and Pluto. *Icarus* 127, 354–378.
- 986 Reuter, D.C., Stern, S.A., Scherrer, J., Jennings, D.E., Baer, J.W., Hanley, J., Hardaway, L., Lunsford, A., McMuldrosch, S.,
987 Moore, J., et al., 2008. Ralph: A visible/infrared imager for the New Horizons Pluto/Kuiper belt mission. *Space Science*
988 *Reviews* 140, 129–154.
- 989 Sagan, C., Khare, B., 1979. Tholins: Organic chemistry of interstellar grains and gas. *Nature* 277, 102–107.
- 990 Sasaki, T., Kanno, A., Ishiguro, M., Kinoshita, D., Nakamura, R., 2004. Search for nonmethane hydrocarbons on Pluto. *The*
991 *Astrophysical Journal Letters* 618, L57.
- 992 Schmitt, B., Philippe, S., Grundy, W., Reuter, D., Cote, R., Quirico, E., Protopapa, S., Young, L., Binzel, R., Cook, J.,
993 Cruikshank, D., Dalle Ore, C., A.M., E., Ennico, K., Howett, C., Jennings, D., Linscott, I., Lunsford, A., Olkin, C., Parker,
994 A., Parker, J., Singer, K., Spencer, J., Stansberry, J., Stern, S., Tsang, C., Verbiscer, A., Weaver, H., the New Horizons Team,
995 2017. Physical state and distribution of materials at the surface of Pluto from New Horizons LEISA imaging spectrometer.
996 *Icarus* 287 , 229–260.
- 997 Sciamma-O'Brien, E., Dahoo, P.R., Hadamcik, E., Carrasco, N., Quirico, E., Szopa, C., Cernogora, G., 2012. Optical constants
998 from 370 nm to 900 nm of Titan tholins produced in a low pressure RF plasma discharge. *Icarus* 218 , 356–363.
- 999 Sekine, Y., Genda, H., Kamata, S., Funatsu, T., 2017. The Charon-forming giant impact as a source of Pluto's dark
1000 equatorial regions. *Nature Astronomy* 1, 1–6.
- 1001 Stern, S., Bagenal, F., Ennico, K., Gladstone, G., Grundy, W., McKinnon, W., Moore, J., Olkin, C., Spencer, J., Weaver, H.,
1002 et al., 2015. The Pluto system: Initial results from its exploration by New Horizons. *Science* 350.
- 1003 Szopa, C., Cernogora, G., Boufendi, L., Correia, J.J., Coll, P., 2006. PAMPRE: A dusty plasma experiment for Titan's tholins
1004 production and study. *Planetary and space Science* 54, 394–404.
- 1005 Trotta, F., 1996. Détermination des constantes optiques de glaces dans l'infrarouge moyen et lointain: application aux grains
1006 du milieu interstellaire et des enveloppes circumstellaires. Ph.D. thesis. Université Joseph Fourier (Grenoble).
- 1007 Verbiscer, A., Showalter, M., Buie, M., Helfenstein, P., 2019. The Pluto System at True Opposition. *LPICo* 2133, 7050.
- 1008 Webber, W., Yushak, S., 1983. A measurement of the energy spectra and relative abundance of the cosmic-ray H and He
1009 isotopes over a broad energy range. *The Astrophysical Journal* 275, 391–404.
- 1010 Wong, M.L., Fan, S., Gao, P., Liang, M.C., Shia, R.L., Yung, Y.L., Kammer, J.A., Summers, M.E., Gladstone, G.R., Young,
1011 L.A., et al., 2017. The photochemistry of Pluto's atmosphere as illuminated by New Horizons. *Icarus* 287, 110–115.
- 1012 Workman, J., 1996. Interpretive Spectroscopy for Near Infrared. *Applied Spectroscopy Reviews* , 251–320.
- 1013 Young, L.A., Kammer, J.A., Steffl, A.J., Gladstone, G.R., Summers, M.E., Strobel, D.F., Hinson, D.P., Stern, S.A., Weaver,
1014 H.A., Olkin, C.B., et al., 2018. Structure and composition of Pluto's atmosphere from the New Horizons solar ultraviolet
1015 occultation. *Icarus* 300, 174–199.
- 1016 Ziegler, J., Manoyan, J., 1988. The stopping of ions in compounds. *Nuclear Instruments and Methods in Physics Research*
1017 *Section B: Beam Interactions with Materials and Atoms* 35, 215–228.

1018 Appendices

1019 A. Inversion of the Hapke model

1020 This appendix describes how to invert Hapke model, in order to extract some surface parameters of
1021 interest from reflectance measurements.

1022 A.1. Estimating the single scattering albedo and phase function

1023 As mentioned in Section 5.5, a linearised least-squares method can be used to invert Hapke model and
1024 retrieve the single scattering albedo and phase function from the tholins reflectance spectra.

1025 The linearised least-squares method is by definition an iterative process. The non-linear relation between
 1026 the parameters to estimate (parameters vector \mathbf{x}) and the observations (here reflectance values, concatenated
 1027 in an observations vector \mathbf{y}) can be written as follows:

$$\mathbf{y} = \mathbf{F}(\mathbf{x})\mathbf{x}, \quad (14)$$

1028 where the matrix $\mathbf{F}(\mathbf{x})$ represents the available model linking the observations to the parameters. From
 1029 the Taylor series of the above equation, a first order approximation can be derived for the deviation in the
 1030 observations which is expected from a small change in the parameters:

$$\delta\mathbf{y} = \left. \frac{\partial\mathbf{F}(\mathbf{x})}{\partial\mathbf{x}} \right|_{\mathbf{x}=\mathbf{x}^*} \delta\mathbf{x}, \quad (15)$$

1031 where \mathbf{x}^* is the current best estimate of the parameters vector \mathbf{x} . To simplify the notations, the partial
 1032 derivatives matrix \mathbf{H} (also referred to as the normal matrix) is introduced, as:

$$\mathbf{H}(\mathbf{x}^*) = \left. \frac{\partial\mathbf{F}(\mathbf{x})}{\partial\mathbf{x}} \right|_{\mathbf{x}=\mathbf{x}^*}. \quad (16)$$

1033 The previous step (Equation 15) is necessary to linearise the problem. The successive updates which
 1034 need to be applied to the parameters vector, starting from an initial guess \mathbf{x}_0 , are given by

$$\delta\mathbf{x}_{i+1} = \left[(\mathbf{H}(\mathbf{x}_i))^T \mathbf{H}(\mathbf{x}_i) \right]^{-1} (\mathbf{H}(\mathbf{x}_i))^T \delta\mathbf{y}_i, \quad (17)$$

1035 where $\delta\mathbf{y}_i$ is the difference between the actual reflectance data and the simulated reflectance values
 1036 obtained with the former estimate of the parameters vector \mathbf{x}_i .

1037 The parameters to be estimated in our particular problem are the single scattering albedo ω (as a function
 1038 of the wavelength λ) and the phase function P which depends on the phase angle g . The model relating
 1039 $\omega(\lambda)$ and $P(g)$ to the expected reflectance is the simplified Hapke model (see Equation 1). The least-squares
 1040 inversion as described in Equation 17 requires the computation of the normal matrix \mathbf{H} defined by Equation
 1041 16. Consequently, the partial derivatives of the simulated reflectance $r(i, e, g, \lambda)$ with respect to both $\omega(\lambda)$
 1042 and $P(g)$ need to be computed. Let us first define the function $\alpha(\omega, \mu_0, \mu)$ as the product of the two multiple
 1043 scattering terms in Equation 1:

$$\begin{aligned} \alpha(\omega, \mu_0, \mu) &= H(\omega, \mu_0)H(\omega, \mu) \\ &= \frac{1 + 2\mu_0}{1 + 2\mu_0\sqrt{1-\omega}} \times \frac{1 + 2\mu}{1 + 2\mu\sqrt{1-\omega}}. \end{aligned} \quad (18)$$

1044 Then, the derivative of the reflectance with respect to the single scattering albedo, for a given value of
 1045 the wavelength λ , can be computed as follows:

$$\begin{aligned} &\left. \frac{\partial r(i, e, g, \lambda)}{\partial\omega} \right|_{\lambda} \\ &= \frac{\partial}{\partial\omega} \left(\frac{\omega}{4\pi} \frac{\mu_0}{\mu_0 + \mu} [P(g) + \alpha(\omega, \mu_0, \mu) - 1] \right) \\ &= \frac{\mu_0}{4\pi(\mu_0 + \mu)} \\ &\quad \times \left[P(g) - 1 + \alpha(\omega, \mu_0, \mu) + \omega \frac{\partial\alpha(\omega, \mu_0, \mu)}{\partial\omega} \right], \end{aligned} \quad (19)$$

1046 where the partial derivative of the function $\alpha(\omega, \mu_0, \mu)$ can be expressed as

$$\begin{aligned} & \frac{\partial \alpha(\omega, \mu_0, \mu)}{\omega} \\ &= (1 + 2\mu_0)(1 + 2\mu) \\ & \quad \times \left[\frac{\frac{\mu_0 + \mu}{\sqrt{1 - \omega}} + 4\mu_0\mu}{(1 + 2(\mu_0 + \mu)\sqrt{1 - \omega} + 4\mu_0\mu(1 - \omega))^2} \right]. \end{aligned} \tag{20}$$

1047 Finally, the partial derivative of the reflectance with respect to the phase function P is

$$\left. \frac{\partial r(i, e, g, \lambda)}{\partial P} \right|_g = \frac{\omega}{4\pi} \frac{\mu_0}{\mu_0 + \mu}, \tag{21}$$

1048 assuming the phase angle g is constant.

1049 After a few iterations, the linearised least-squares inversion described above converges towards an esti-
1050 mated solution for the single scattering albedo and the phase function.

1051 A.2. Extracting the optical constants

1052 As already discussed in Section 4.2.3, the Maxwell-Garnett model requires the optical constants of the
1053 tholins as input. However, the least-squares inversion of the simplified Hapke model described in Appendix
1054 A.1 only provides an estimate of the single scattering albedo $\omega(\lambda)$ and phase function $P(g)$ for the laboratory
1055 synthesised tholins.

1056 The highly non-linear relation between the single scattering albedo ω and optical constants n and k (see
1057 Equation 2) does not allow for a straight-forward determination of the tholins optical constants from ω .

1058 The spectral information is mostly carried by k , except for strong fundamental bands. The near-infrared
1059 spectral range covered by LEISA spectra corresponds to the domain of overtone and combination bands.
1060 Variations of the refractive index n are therefore expected to not exceed a few percents. On the other hand,
1061 the very strong band in the UV-visible responsible for the red slope should lead to a large change in the
1062 refractive index n in the visible. Using the n values provided in Khare et al. (1984) aims at taking this
1063 variation into account.

1064 From these assumed n values, we estimate the corresponding values of k that would match the single
1065 scattering albedo ω . To compute k as a function of the wavelength, the expression giving the single scattering
1066 albedo as a function of n and k (Equations 7 and 8) must be inverted for each wavelength. Because the
1067 expression for ω is highly non-linear, a linearised least-squares method can be employed, exactly similar to
1068 the one presented in Appendix A.1.

1069 The observations are here the single scattering albedo values for all wavelengths of interest, while the
1070 parameters to be estimated are the associated k values. The normal matrix \mathbf{H} contains the partial derivatives
1071 of ω with respect to k , evaluated separately at each wavelength. The iterative linearised least-squares method
1072 converges within a few iterations and provides estimates for the k values.

1073 A.3. Tabulated results of the Hapke model inversion

1074 This appendix provides the tabulated values for the single scattering albedo ω and phase function P
1075 obtained after performing the inversion of the Hapke model as described in Appendix A.1. Results are
1076 reported for both 5%CH₄ and 1%CH₄ tholins, in Tables A.1 and A.2 for ω and P , respectively. Table A.3
1077 contains the optical constants extracted from the single scattering albedo, as described in Appendix A.2. k
1078 values are also displayed as a function of the wavelength in Figure A.1.

1079 Again, it must be highlighted that those parameters are determined in a purely numerical way. They
1080 need to be used carefully, keeping in mind the inherent lack of physical meaning behind the least-squares
1081 inversion of our models.

1082 These data are also available through the GhoSST database in SSHADE infrastructure of solid spec-
1083 troscopy: https://doi.org/10.26302/SSHADE/EXPERIMENT_BS_20201201_001 (Fayolle et al., 2018).

$\text{N}_2:\text{CH}_4 = 95:5$ tholins				$\text{N}_2:\text{CH}_4 = 99:1$ tholins			
$\lambda[\mu\text{m}]$	$\omega[-]$	$\lambda[\mu\text{m}]$	$\omega[-]$	$\lambda[\mu\text{m}]$	$\omega[-]$	$\lambda[\mu\text{m}]$	$\omega[-]$
0.40	0.1209	1.46	0.9957	0.40	0.0746	1.46	0.9921
0.44	0.1904	1.50	0.9948	0.44	0.1116	1.50	0.9914
0.48	0.2685	1.54	0.9953	0.48	0.1521	1.54	0.9924
0.52	0.3742	1.58	0.9963	0.52	0.2142	1.58	0.9939
0.56	0.4906	1.62	0.9967	0.56	0.2937	1.62	0.9946
0.60	0.6042	1.66	0.9966	0.60	0.3863	1.66	0.9947
0.64	0.7056	1.70	0.9956	0.64	0.4835	1.70	0.9943
0.68	0.7901	1.74	0.9950	0.68	0.5787	1.74	0.9938
0.72	0.8529	1.78	0.9950	0.72	0.6621	1.78	0.9934
0.76	0.8983	1.82	0.9956	0.76	0.7333	1.82	0.9937
0.80	0.9303	1.86	0.9955	0.80	0.7929	1.86	0.9933
0.84	0.9522	1.90	0.9885	0.84	0.8412	1.90	0.9846
0.88	0.9674	1.94	0.9781	0.88	0.8801	1.94	0.9707
0.92	0.9778	1.98	0.9762	0.92	0.9102	1.98	0.9677
0.96	0.9846	2.02	0.9776	0.96	0.9328	2.02	0.9678
1.00	0.9893	2.06	0.9794	1.00	0.9505	2.06	0.9695
1.04	0.9925	2.10	0.9797	1.04	0.9635	2.10	0.9695
1.08	0.9945	2.14	0.9789	1.08	0.9724	2.14	0.9684
1.12	0.9959	2.18	0.9756	1.12	0.9792	2.18	0.9643
1.16	0.9967	2.22	0.9722	1.16	0.9841	2.22	0.9597
1.20	0.9973	2.26	0.9684	1.20	0.9876	2.26	0.9586
1.24	0.9978	2.30	0.9685	1.24	0.9903	2.30	0.9617
1.28	0.9981	2.34	0.9712	1.28	0.9921	2.34	0.9644
1.32	0.9983	2.38	0.9699	1.32	0.9936	2.38	0.9626
1.38	0.9980	2.42	0.9653	1.38	0.9938	2.42	0.9555
1.42	0.9970	2.46	0.9586	1.42	0.9936	2.46	0.9446
		2.50	0.8903			2.50	0.8614

Table A.1: Single scattering albedo obtained from the inversion of the Hapke model, for 5%CH₄ and 1%CH₄ tholins.

$\text{N}_2:\text{CH}_4 = 95:5$ tholins		$\text{N}_2:\text{CH}_4 = 99:1$ tholins	
g [°]	P [-]	g [°]	P [-]
10	2.1757	10	2.2954
20	1.7848	20	1.9600
30	1.5956	30	1.7704
40	1.3621	40	1.5006
50	1.1413	50	1.2421
60	0.8577	60	0.9117
70	0.9943	70	1.0403
80	0.8412	80	0.8932
90	0.7898	90	0.8369
100	0.7513	100	0.8128
110	0.6720	110	0.6953
120	0.6967	120	0.7009
130	0.7506	130	0.7540

Table A.2: Phase function obtained from the inversion of Hapke model, for 5%CH₄ and 1%CH₄ tholins.

1084 B. Optimisation process

1085 This appendix provides more details about the optimisation problem introduced in Section 4.3 and about
 1086 the optimisation algorithm selected to tackle it.

1087 B.1. Definition of the optimisation problem

1088 For this particular problem, the optimisation objective (*i.e.* variable to be minimised) was defined as
 1089 the χ^2 between the simulated reflectance and the New Horizons spectrum.

1090 As a reminder, below are listed the design parameters (*i.e.* free parameters) whose values were tuned
 1091 by the optimisation algorithm to find the best match between the simulated spectra and the New Horizons
 1092 data:

- 1093 • mass ratio m_j of each of the chemical species within the intimate mixture of the refractories spatial
 1094 unit (H₂O, C₂H₆, CH₃OH, tholins);

Testing tholins as analogues of the dark reddish material covering Pluto's Cthulhu region

$\lambda[\mu\text{m}]$	$n[-]$ (Khare et al., 1984)	$k_{95.5}[-]$	$k_{99.1}[-]$
0.50	1.7075	1.1015e-1	2.6428e-1
0.54	1.7032	7.3915e-2	1.6818e-1
0.58	1.6973	5.0537e-2	1.1757e-1
0.62	1.6905	3.4867e-2	8.4720e-2
0.66	1.6841	2.4006e-2	6.2135e-2
0.70	1.6785	1.6544e-2	4.6150e-2
0.74	1.6736	1.1526e-2	3.5007e-2
0.78	1.6690	8.0749e-3	2.6709e-2
0.82	1.6649	5.6880e-3	2.0416e-2
0.86	1.6611	4.0332e-3	1.5621e-2
0.90	1.6576	2.8385e-3	1.1866e-2
0.94	1.6539	2.0318e-3	9.0712e-3
0.98	1.6510	1.4784e-3	6.9406e-3
1.02	1.6500	1.0623e-3	5.2102e-3
1.06	1.6500	7.9285e-4	4.0014e-3
1.10	1.6500	6.0408e-4	3.1225e-3
1.14	1.6500	4.7837e-4	2.4398e-3
1.18	1.6500	4.1323e-4	1.9458e-3
1.22	1.6492	3.4153e-4	1.5600e-3
1.26	1.6463	2.9543e-4	1.2884e-3
1.30	1.6428	2.6711e-4	1.0812e-3
1.34	1.6403	2.7703e-4	9.7626e-4
1.40	1.6400	3.8951e-4	9.9516e-4
1.44	1.6400	6.2087e-4	1.2133e-3
1.48	1.6400	8.5324e-4	1.4712e-3
1.52	1.6400	9.0818e-4	1.4798e-3
1.56	1.6400	7.6851e-4	1.2438e-3
1.60	1.6400	6.3797e-4	1.0640e-3
1.64	1.6400	6.2505e-4	1.0201e-3
1.68	1.6400	7.7079e-4	1.0869e-3
1.72	1.6400	9.5738e-4	1.2050e-3
1.76	1.6400	1.0499e-3	1.3414e-3
1.80	1.6400	1.0007e-3	1.3817e-3
1.84	1.6373	8.9699e-4	1.3440e-3
1.88	1.6300	1.4630e-3	2.0890e-3
1.92	1.6300	4.1545e-3	5.5626e-3
1.96	1.6300	5.5260e-3	7.4896e-3
2.00	1.6300	5.6724e-3	8.0113e-3
2.04	1.6300	5.2411e-3	7.7560e-3
2.08	1.6300	5.1284e-3	7.7276e-3
2.12	1.6300	5.2320e-3	7.9533e-3
2.16	1.6300	5.8724e-3	8.8104e-3
2.20	1.6300	7.0284e-3	1.0365e-2
2.24	1.6294	8.0748e-3	1.1421e-2
2.28	1.6269	9.0836e-3	1.1346e-2
2.32	1.6236	8.4631e-3	1.0471e-2
2.36	1.6209	8.4280e-3	1.0486e-2
2.40	1.6200	9.5207e-3	1.2080e-2
2.44	1.6199	1.1541e-2	1.5279e-2
2.48	1.6191	1.4947e-2	2.0615e-2

Table A.3: Optical constants obtained from the numerical inversion described in Appendix A.2, for 5%CH₄ and 1%CH₄ tholins.

- 1095 • mean particle diameter for each of the chemical species (H₂O, C₂H₆, CH₃OH, tholins, CH₄);
- 1096 • spatial ratio between the two units (the refractories and the volatiles ones);
- 1097 • spatial fraction of tholins in icy grains when the Maxwell-Garnett model is used (Section 6.2.2). If so,
- 1098 the mean particle diameter and mass fraction associated with tholins are removed from the list of the
- 1099 design variables;
- 1100 • macroscopic porosity parameter K .

1101 All the mass and spatial ratios are by definition ranging from 0 to 1, which is also the case for the porosity
1102 parameter K . Additionally, the sum of the mass fractions of the refractory species covering one of two
1103 spatial units (see Figures 2 and 3) must be equal to 1. Finally, the mean particle diameters were constrained
1104 between 0.1 μm and 100 μm .

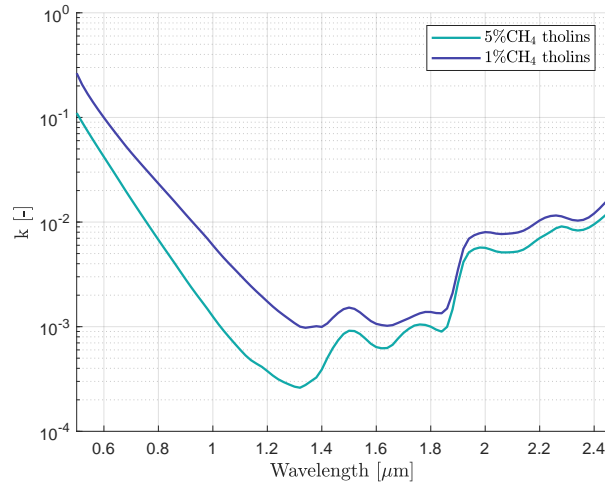


Figure A.1: k values for both 5%CH₄ and 1%CH₄ tholins, obtained from the numerical inversion described in Appendix A.2.

B.2. Selection of the optimisation algorithm

To conduct the optimisation process, we used the PAGMO toolbox developed by the Advanced Concepts Team (ACT) at ESA, which offers a wide range of optimisation algorithms (in C++). The documentation can be accessed at <https://esa.github.io/pagmo2/>.

As mentioned in Section 4.3, the performance of several global optimisation algorithms was assessed in terms of convergence and computational efficiency for our particular optimisation problem. The simple genetic algorithm, differential algorithm, predator-swarm algorithm, and artificial bee colony were tested. Those are all population-based evolutionary algorithms.

Except for the artificial bee colony algorithm, the other ones all achieved convergence (verified by re-conducting the optimisation process with different random seeds). The simple genetic algorithm offered the best trade-off: it seemed to provide a good approximation of the global optimum within a reasonable computational time. The efficiency of the genetic algorithm was of particular relevance for this work, as both the number of design parameters and the associated search space were large, while computational capabilities were limited. For these reasons, this algorithm was selected to tackle the optimisation problem described in Appendix B.1.

The simple genetic algorithm relies on Darwin's natural selection principle, and more precisely on the "survival of the fittest" concept (*e.g.* Goldberg, 1989). As for any other evolutionary algorithm, an initial population of individuals (*i.e.* solutions, or combinations of design parameters) is generated. The "fitness" of each of these individuals is computed, as being equal to the value of the optimisation objective corresponding to the particular set of design parameters defining the individual. The population then evolves to form a second generation. Mimicking the evolution of populations according to evolutionary theories, parents are selected among the current population of solutions and each child individual is computed as a mix between the two sets of design parameters originating from its two parents. Following the natural selection principle, individuals associated with a good fitness value (*i.e.* for which the value of the optimisation objective is lower) are more likely to be selected as parents among a given generation, and thus to propagate the good performing design parameters defining them to the next generation. As generations keep being generated, the best identified fitness value tends to get closer to the global optimum and the "fittest" individuals thus approach the best set of design parameters. To guarantee a good sampling of the research space, the population size (*i.e.* number of individuals per generation) should not be chosen too small. Additionally, mutations are introduced from one generation to the next to increase the diversity within the population, again based on what is observed in natural species evolution.